Winter 1997

Kramers-Kronig Anomalous Dispersion on Single-Mode Fiber-Optic Couplers and Tapers

Arnel C. Lavarias
Old Dominion University

KRAMERS-KRONIG ANOMALOUS DISPERSION ON SINGLE-MODE FIBER OPTIC COUPLERS AND TAPERS

by

Arnel C. Lavarias
B.S.E.E. May 1993, Old Dominion University
M.S.E.E. May 1995, Old Dominion University

A Dissertation Submitted to the Faculty of
Old Dominion University in Partial Fulfillment of the
Requirements for the Degree of

DOCTOR OF PHILOSOPHY

ELECTRICAL ENGINEERING

OLD DOMINION UNIVERSITY
December 1997

Approved by:

Sacharia Albin

John B. Cooper

Amin N. Dharamsi

Linda L. Vahala

ABSTRACT

KRAMERS-KRONIG ANOMALOUS DISPERSION ON SINGLE-MODE FIBER OPTIC COUPLERS AND TAPERS

Arnel Cabasa Lavarias
Old Dominion University, 1997
Director: Dr. Sacharia Albin

The Kramers-Kronig relations couple the real and imaginary part of the dielectric constant of a medium, namely the refractive index $n(\omega)$ and the extinction coefficient $\kappa(\omega)$. Changes in $n(\omega)$ due to normal and anomalous dispersion (Kramers-Kronig effect) are investigated for the first time using fiber optic couplers and tapers. Kramers-Kronig effect is induced by evanescent wave absorption in these devices. Couplers and tapers have oscillatory spectral outputs that are highly sensitive to the refractive index of the surrounding medium. Theoretical modeling of the Kramers-Kronig effect on couplers and tapers shows two distinct effects. First, the spectral outputs of these devices show a decrease in intensity due to evanescent wave absorption. Second, the spectral maxima and minima are shifted in wavelength due to Kramers-Kronig effect. Experimental studies clearly demonstrate Kramers-Kronig anomalous dispersion on fiber optic couplers and tapers. These devices are shown to be useful as chemical sensors.

ACKNOWLEDGMENTS

First and foremost, I would like to thank God for giving me the strength and the will to accomplish this very difficult task.

I would like to thank Dr. Sacharia Albin for giving me the confidence to fulfill a very important goal in my life. His wisdom, guidance, and especially his patience were invaluable in this research. I would also like to thank Dr. Amin Dharamsi, Dr. Linda Vahala, and Dr. John Cooper for taking time out of their busy schedules to help me bring this research to a conclusion.

A very special note of thanks goes out to Dr. Jianli Zheng. His experience and insights in fiber optics research proved to be most valuable and often times ingenious. I would also like to acknowledge Weihai Fu, Randy Cole, Todd Lindley, Willie Bowen, John Hagwood, and Melanie Ratcliff. I have enjoyed working and talking with each of them, and I am thankful to have learned so much about so many things from them.

I am indebted to Dr. Robert Rogowski, Dr. Claudio Egalon, and Carl Aude of NASA Langley Research Center for their scientific discussions and assistance. I acknowledge with thanks the fellowship by NASA Graduate Student Researchers Program, under contract number NGT-70308.

I would also like to acknowledge the Virginia Space Grant Consortium Aerospace Graduate Research Fellowship, which was also vital to the completion of this research.

Finally, I would like to thank my family and friends for believing in me.

TABLE OF CONTENTS

LIST OF TABLES

TABLE PAGE

LIST OF FIGURES

FIGURE PAGE

CHAPTER I

INTRODUCTION

The Kramers-Kronig relations are a subset of the more general dispersion relations. They were derived by H. A. Kramers in 1927 and R. de L. Kronig in 1926 independently. These equations give the relationship between the real and imaginary parts of the dielectric constant $\varepsilon(\omega)$,

$$n(\omega) = 1 + \frac{2}{\pi} P \int_0^{\infty} \frac{\omega' \kappa(\omega')}{\omega'^2 - \omega^2} d\omega' \tag{1}$$

$$\kappa(\omega) = \frac{-2\omega}{\pi} P \int_0^{\infty} \frac{n(\omega') - 1}{\omega'^2 - \omega^2} d\omega' \tag{2}$$

where $n(\omega)$ is the refractive index and $\kappa(\omega)$ is the extinction coefficient. Thus, empirical knowledge of $\kappa(\omega)$ from absorption studies allows calculation of the refractive index $n(\omega)$ using the Kramers-Kronig relations.

The Kramers-Kronig relations have been applied to infrared transmission spectra to extract complex refractive index of thin film materials [1]. These relations have also been applied to reflection spectra of thin films to obtain the complex refractive index [2] since the real part of the complex reflectivity is directly measured as the reflectivity. Analysis of attenuated total reflection (ATR) spectra of thin films using Kramers-Kronig relations similarly yields complex refractive index measurements, but without prior knowledge of thin film thickness. Because absorption studies yield $\kappa(\omega)$, solid, liquid, and gaseous media can be analyzed using Kramers-Kronig relations so that $n(\omega)$ can be obtained.

1.1 Fiber Optic Sensors

Sensing of a variable is essential for the measurement and control of any process. Pressure, temperature, flow, displacement, rotation, and others, act to directly modulate light in two distinct ways in fiber optic sensors (FOS). Extrinsic FOS are distinguished by the characteristics that the sensing takes place external to the fiber. The optical fiber only acts as information carriers to and from the sensing region, or transducer, as shown in Figure 1a [3]. This transducer modulates the light when the process variable acts upon it. FOS that fall in this category include temperature sensors based on fluorescence or absorption band edge of a material, pressure sensors based on reflection or transmission, and flow sensors using laser Doppler velocimetry. On the other hand, in an intrinsic FOS, the environmental effect directly affects the light-guiding properties of the optical fiber as the light traverses the fiber, as shown in Figure 1b [3]. A transducer is not necessary since sensing takes place within the fiber itself. Examples of this type include Rayleigh- and Raman-based temperature sensors, microbend sensors sensitive to strain and pressure, and interferometric-based sensors for measuring rotation, acceleration, strain, temperature, electric and magnetic fields.

Intrinsic FOS are particularly useful for monitoring process variable which change the light propagation properties of the fiber. An important class of such sensors is based on changes in index of refraction. These FOS are important in measuring parameters such as fluid level, temperature, species concentration, and refractive index. The light guiding properties of a cladding-stripped optical fiber depends on the refractive index of the material surrounding the fiber. From Snell's law,

$$n_1 \sin \theta_1 = n_2 \sin \theta_2 \tag{3}$$

where n_1 and θ_1 are the refractive index and angle of incidence within the fiber and n_2 and θ_2 are the refractive index and angle of transmission in the surrounding medium. Processes which alter n_1 or n_2, such as introducing an absorbing material in the core or immersing the unclad fiber in a liquid, affect the condition for total internal reflection within the fiber, and this can cause light to couple out of the fiber core into the surrounding medium [4, 5].

1.2 Optical Absorption and Dispersion

The optical constants, viz. index of refraction and extinction coefficient, of a material are fundamental parameters which depend on wavelength. Although these parameters cannot be determined easily, simple reflection or transmission spectra related to these parameters can easily be recorded. Normal dispersion and anomalous dispersion, or Kramers-Kronig effect, in the index of refraction will occur near an absorption band, and this dispersion can be very large for very sharp bands. This change in refractive index will cause a change in reflection and transmission measurements. Often, the refractive index of a material is assumed constant near the absorption wavelength, leading to errors in reflection and transmission measurements [6].

Spectroscopic measurements typically measure absorption bands modified by dispersion effects or reflection spectra modified by both absorption and dispersion effects. Measurements taken from internal reflectance spectroscopy and attenuated total reflectance of various materials tend to show these effects for strong absorption bands. Infrared reflectance measurements of semiconductor thin films yield a pattern of maxima and minima as a function of wavelength due to interference at the thin film boundaries. This information is used to determine film thickness [7], but the refractive index is

assumed to have a constant value over the range of wavelengths used in the measurements. Therefore, an absorption band in the wavelength range will lead to normal and anomalous dispersion, leading to errors in the calculated thin film thickness.

The anomalous dispersion, or Kramers-Kronig effect, associated with the presence of an absorption band will also affect the performance of FOS based on refractive index changes. Sensors using fiber optic couplers and tapers are particularly affected by this effect because the light-guiding properties, as well as the spectral outputs, of these optical components depend on the refractive indices of the fiber and the environment surrounding the component. Up to now, no research has been reported to show the effect of anomalous dispersion on fiber optic couplers and tapers. Hence, sensors using couplers and tapers may have an inherent error when optical dispersion is present.

1.3 Scope of Research

Refractive index is an important parameter that should be monitored in the operation of many FOS. Changes in refractive index due to normal and anomalous dispersion near an absorption line have been researched, however, these effects have not been studied in conjunction with the operation of fiber optic couplers and tapers. Thus, the objective of this research is to investigate how the Kramers-Kronig effect (i.e. normal and anomalous dispersion due to the presence of an absorption line) affects the properties of fiber optic couplers and tapers. More specifically, theoretical modeling of the Kramers-Kronig effect on couplers and tapers will be conducted in Chapter II. Experiments to verify the theoretical modeling will be presented in Chapter III. Finally, a

discussion of the results and concluding remarks and applications for this type of fiber optic sensor will be given in Chapter IV and V, respectively.

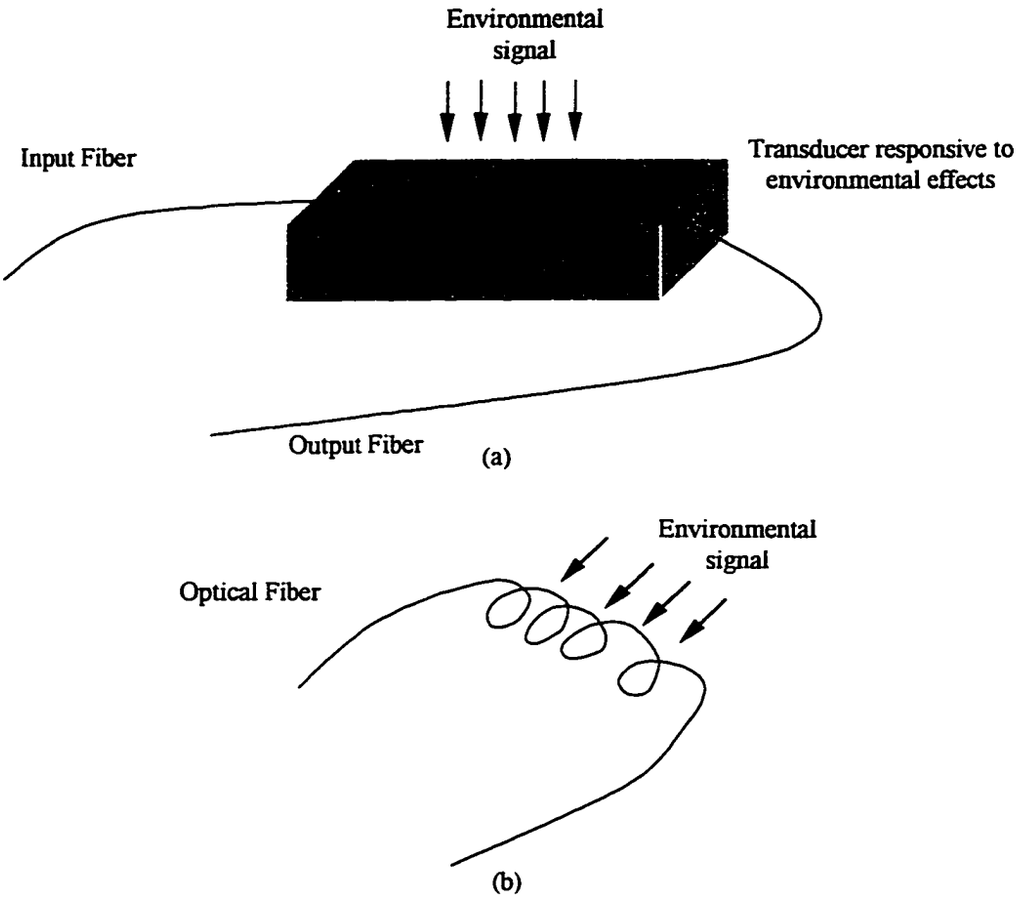

Figure 1: (a) Extrinsic FOS consisting of input and output fibers to carry the light to and from the "black box". (b) Intrinsic FOS whose light-guiding properties are modulated directly by the environmental signal.

CHAPTER II

THEORETICAL BACKGROUND

Several FOS rely upon couplers and tapers as sensing devices, and the effect of Kramers-Kronig anomalous dispersion on such devices has not previously been studied. In this chapter, a theoretical background of Kramers-Kronig effect will be discussed first. A thorough background of the light-guiding properties of fiber optic couplers and tapers will be discussed next. Couplers and tapers will be treated separately in the analysis. Fiber optic evanescent wave absorption is described since absorption and dispersion are coupled by the Kramers-Kronig effect. The change in the output characteristics of couplers and tapers due to Kramers-Kronig effect will be evaluated theoretically.

2.1 Optical Absorption, Dispersion, and the Kramers-Kronig Effect

The classical theory for the propagation of light through dielectric media was first proposed by Lorentz and Drude to account for the absorption, dispersion, and reflection of light. Despite some fundamental differences between classical and quantum mechanical theory, the classical theory is still used since it gives essentially the same results concerning the interaction of electromagnetic radiation on a dielectric material. The classical theory is very useful in interpreting results of optical measurements. Several well-known relations, including the Clausius-Mosotti relation and the Kramers-Kronig relation, follow directly from this theory.

Using Maxwell's equations, the interaction of electromagnetic radiation with a dielectric medium can be expressed as:

$$\nabla \cdot \bar{E} = 0$$
$$\nabla \cdot \bar{B} = 0$$
$$\nabla \times \bar{E} = -\frac{\partial \bar{B}}{\partial t} \tag{4}$$
$$\nabla \times \bar{H} = \varepsilon_o \frac{\partial \bar{E}}{\partial t} + (\frac{\partial \bar{P}}{\partial t} + \bar{J})$$

where $\bar{P}$ is the polarization and $\bar{J}$ is the current density. By looking for the plane wave solutions in the form

$$\bar{E} = \bar{E}_o \exp[i(\bar{k}z - \omega t)] \tag{5}$$

and defining

$$(\bar{k})^2 = \omega^2 \frac{(\bar{n})^2}{c^2} \tag{6}$$

$$\bar{n} = n - i\kappa \tag{7}$$

where z is the direction of wave propagation, $\bar{k}$ is the complex wave vector, ω is the angular frequency, and c is the speed of light in vacuum, the solution to Maxwell's equations is

$$\bar{E} = \bar{E}_o \exp[i(\bar{k}z - \omega t)] = \bar{E}_o \exp[i\omega(\frac{\bar{n}z}{c} - t)]. \tag{8}$$

$\bar{n}$ is the complex index of refraction from which the optical constants n and κ are derived and will affect the way electromagnetic radiation will interact with the dielectric material as it passes through [8]. By applying this equation to the plane-wave solution of Maxwell's equation,

$$\bar{E} = \bar{E}_o \exp\left[\frac{-2\pi\kappa z}{\lambda}\right] \exp\left[i(\frac{2\pi n z}{\lambda} - \omega t)\right]. \tag{9}$$

The first exponential describes the amplitude attenuation of the electromagnetic radiation as it passes through the dielectric material. It is in this term that the attenuation coefficient, or absorption coefficient α, is defined based on the value of κ:

$$\alpha = \frac{4\pi\kappa}{\lambda}. \tag{10}$$

The second exponential describes the phase velocity v of the electromagnetic radiation propagating through the dielectric medium, and it depends on the refractive index n for the dielectric material:

$$v = \frac{c}{n} = \frac{\omega}{2\pi}\frac{\lambda}{n}. \tag{11}$$

Equation 9 does not account for material dispersion when the wave passes through the dielectric medium. However, Lorentz and Drude developed the classical theory of optical dispersion by modeling the medium in which the electrons or ions were represented as classical harmonic oscillators. The response of these charges to the electric field of the light traversing the medium is calculated using the classical equation of motion.

The classical treatment of dispersion begins by considering the forces acting on an electron bound to its nucleus or an ion bound to its lattice site, as shown in Figure 2a [9]. The electron and nucleus act as a dipole creating a dipole moment

$$\bar{p} = -q\bar{r} \tag{12}$$

and a polarization

$$\bar{P} = -Nq\bar{r} = N\bar{p} \tag{13}$$

where N is the number of dipoles per unit volume and q is the electronic charge. The electron and nucleus will be bound with a linear restoring force $-K\bar{r}$ and a damping force $-m\gamma\frac{d\bar{r}}{dt}$, as shown in Figure 2b [9]. γ is the damping coefficient, m is the mass of the electron, and K is the spring constant. The presence of an applied electric field $\bar{E}$ will also produce a force $-q\bar{E}$ on the electron. The massive nucleus is considered

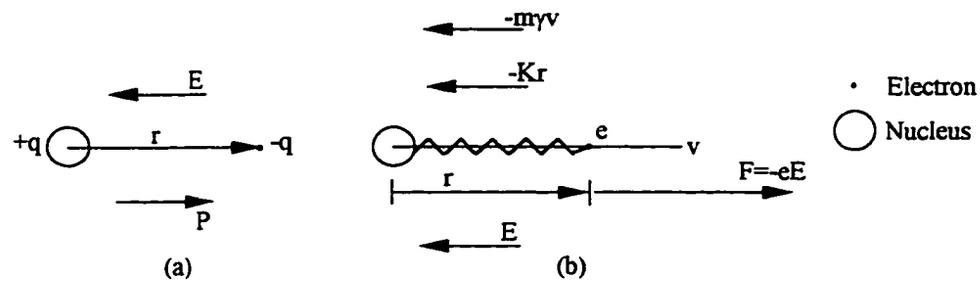

Figure 2: The elementary electric dipole. (a) Alignment with an applied electric field. (b) Forces acting on a dipole when the electric field has the direction indicated.

stationary, and under an applied oscillating electric field, the electron oscillations will extract some energy from the incident field. Hence, the electron acts as a damped harmonic oscillator, and by applying Newton's second law, the equation of motion of the electron in the z-direction is

$$-Kz - m\gamma\frac{dz}{dt} - qE = m\frac{d^2z}{dt^2} \tag{14}$$

where m is the mass of the electron and q is the electronic charge. Since $\omega_o^2 = \frac{K}{m}$, the solution to Equation 14 is

$$z = \frac{\frac{q}{m}E}{\omega_o^2 - \omega^2 + i\gamma\omega}. \tag{15}$$

The problem now lies in trying to relate the electron displacement, z, with the dielectric constant, ε. The dielectric constant is defined from the definition of electric displacement

$$D = \varepsilon E. \tag{16}$$

The electric displacement is also defined as

$$D = \varepsilon_o E + P. \tag{17}$$

Here, ε_o is the permittivity of free space and P is the polarization of the medium, which is defined by

$$P = Nqz \tag{18}$$

where qz is the dipole moment. By substituting Equations 15 and 18 into 17 and equating Equations 16 and 17, the complex dielectric constant becomes:

$$\varepsilon = 1 + \frac{Nq^2}{\varepsilon_o m}\left[\frac{1}{\omega_o^2 - \omega^2 + i\gamma\omega}\right]. \tag{19}$$

Equation 19 is applicable only to a gas medium since it does not account for the interaction of neighboring electric dipoles. The variation of ε with free space wavelength λ is seen by plotting the optical constants n and κ with frequency. Defining $\varepsilon = (n - i\kappa)^2 = (\bar{n})^2$ and using the binomial theorem, the optical constants can be analytically determined:

$$n \approx 1 + \frac{Nq^2}{2\varepsilon_o m}\left[\frac{\left(\lambda_o^2\lambda^2\right)\left(\lambda^2-\lambda_o^2\right)}{4\pi^2c^2\left(\lambda^2-\lambda_o^2\right)^2+\gamma^2\lambda_o^4\lambda^2}\right]$$
$$\kappa \approx \frac{Nq^2}{2\varepsilon_o m}\left[\frac{\gamma\lambda_o^4\lambda^3}{(2\pi c)^3\left(\lambda^2-\lambda_o^2\right)^2+(2\pi c)\left(\gamma^2\lambda_o^4\lambda^2\right)}\right]. \quad (20)$$

The binomial theorem is used under the assumption that

$$\frac{Nq^2}{\varepsilon_o m}\left[\frac{1}{\omega_o^2-\omega^2+i\gamma\omega}\right]<1$$

or, equivalently, $\left(\omega_o^2-\omega^2\right)$ is large. In addition, the damping constant is related to the optical linewidth $\Delta\lambda$ via $\gamma=\frac{2\pi c}{\lambda_o^2}\Delta\lambda$. As an example, a graphical representation of Equations 20 can be obtained for the 1550 nm absorption line of an arbitrary gas with a density of $3\cdot10^{19}$ m^3, as shown in Figure 3a and b. As λ decreases toward the absorption wavelength λ_o, κ exhibits a maximum value, as shown in Figure 3a. However, as λ decreases towards λ_o, n increases, and this is called ***normal dispersion***. When λ passes and becomes less than λ_o, the value of n reaches a maximum, then decreases to a minimum. This behavior of n is called ***anomalous dispersion*** or Kramers-Kronig effect since the value of n decreases with decreasing λ.

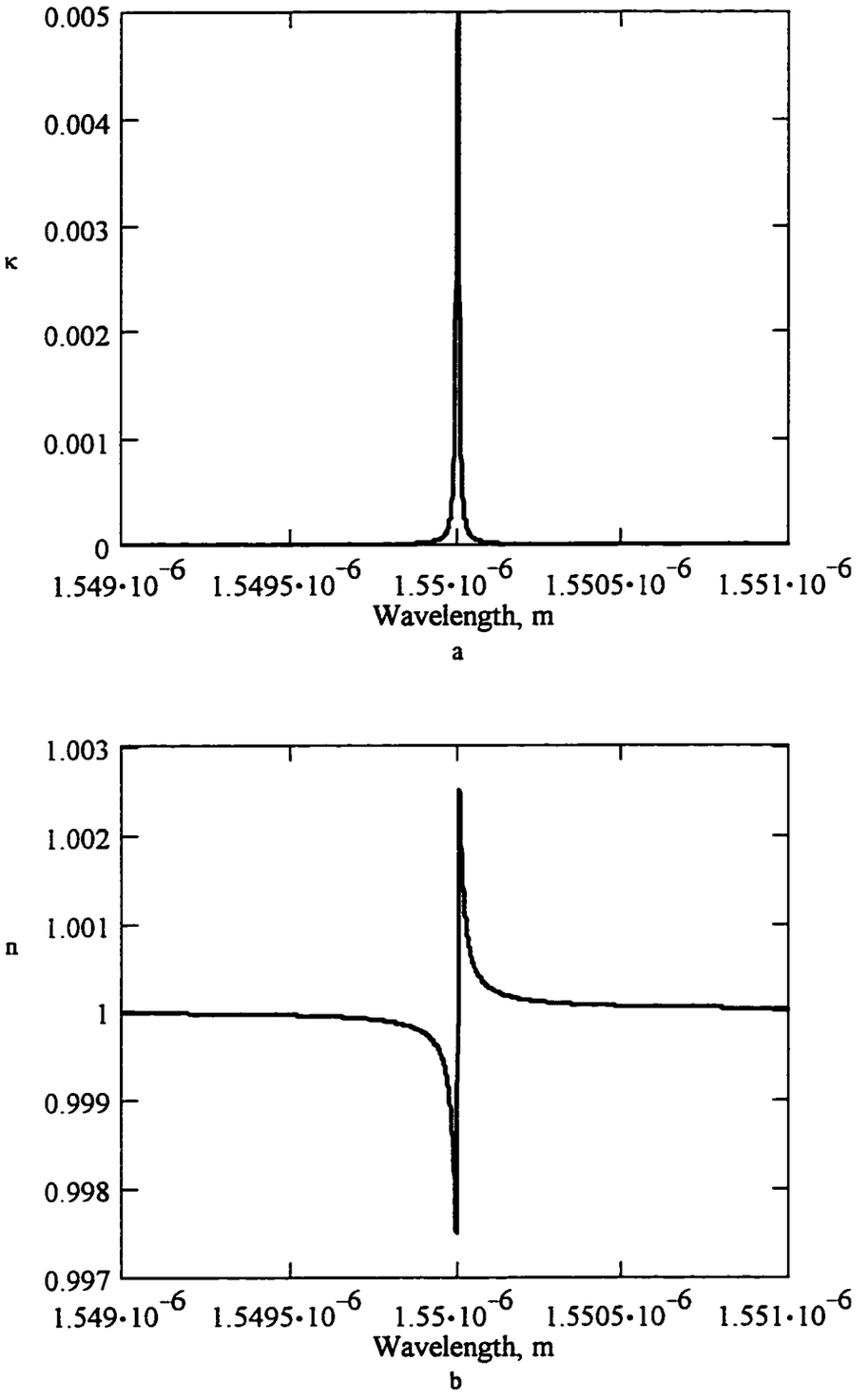

Figure 3: Variation of a) κ and b) n with wavelength for gaseous medium. For these curves, λ_o = 1550 nm, N = $3*10^{19}$ m^{-3}, and $\Delta\lambda$ = 0.01 nm.

Although the complex dielectric constant given by Equation 19 was applicable to gases, the above derivation can also be applied to dense media- liquids and solids- by modifying the equation of motion of the electron. In particular, the equation of motion given by equation 14 must include the interaction of the electron with its neighboring electrons [10]. This is accomplished by replacing the applied electric field term with the Lorentz local field term [10, 11]. The Lorentz local field is comprised of contributions from the applied electric field, the depolarization field due to surface charges, and Lorentz cavity field and is found to be

$$E_L = E + aP \tag{21}$$

where a, for nonpolar dielectrics with cubic symmetry, is $\frac{1}{3\varepsilon_o}$. With this local field replacing the applied electric field E in the equation of motion, it can be shown that the complex dielectric constant becomes

$$\varepsilon = 1 + \frac{4\pi Nq^2}{m}\left[\frac{1}{\left(\omega_o^2 - \omega^2 - \frac{4\pi Nq^2}{3m}\right) + i\gamma\omega}\right]. \tag{22}$$

n and κ can be obtained from Equation 22 and plotted as a function of frequency. By applying complex variable theory, n and κ can be analytically separated from the complex form of ε. They are given in terms of free space wavelength λ as:

$$n = \left[x^2(\lambda) + y^2(\lambda)\right]^{\frac{1}{4}} \cos\left\{\frac{1}{2}\left[\tan^{-1}\left(\frac{-y(\lambda)}{x(\lambda)}\right) - \delta\right]\right\} \tag{23}$$

$$\kappa = -\left[x^2(\lambda) + y^2(\lambda)\right]^{\frac{1}{4}} \sin\left\{\frac{1}{2}\left[\tan^{-1}\left(\frac{-y(\lambda)}{x(\lambda)}\right) - \delta\right]\right\} \tag{24}$$

$$\begin{aligned} \delta &= \pi, \text{if } x(\lambda) < 0 \\ \delta &= 0, \text{if } x(\lambda) > 0 \end{aligned} \tag{25}$$

where x(λ) and y(λ) are defined as

$$\begin{aligned} x(\lambda) &= n^2 + \frac{\left(\frac{Nq^2}{m\varepsilon_o\lambda_o^2}\right) - \frac{1}{3}\left(\frac{Nq^2}{2\pi cm\varepsilon_o}\right)^2 - \left(\frac{Nq^2}{m\varepsilon_o\lambda^2}\right)}{\left[\left(\frac{2\pi c}{\lambda_o^2}\right) - \left(\frac{Nq^2}{6\pi cm\varepsilon_o}\right) - \left(\frac{2\pi c}{\lambda^2}\right)\right]^2 + \left(\frac{\gamma}{\lambda}\right)^2} \\ y(\lambda) &= \frac{\left(\frac{Nq^2}{m\varepsilon_o}\right)\left(\frac{\gamma}{2\pi c\lambda}\right)}{\left[\left(\frac{2\pi c}{\lambda_o^2}\right) - \left(\frac{Nq^2}{6\pi cm\varepsilon_o}\right) - \left(\frac{2\pi c}{\lambda^2}\right)\right]^2 + \left(\frac{\gamma}{\lambda}\right)^2} \end{aligned} \tag{26}$$

Using the same example given in Figure 3, n and κ are obtained as a function of wavelength, as shown in Figure 4a and b. The effect of the dense medium is to shift the resonant frequency to a lower value than that of a gaseous medium. From Equation 22, it is evident that as the concentration of the medium increases, the resonance wavelength of the medium will increase [10, 11]. Note that the wavelength range in Figure 3 is a portion of that shown in Figure 4 to emphasize the shape of κ and n.

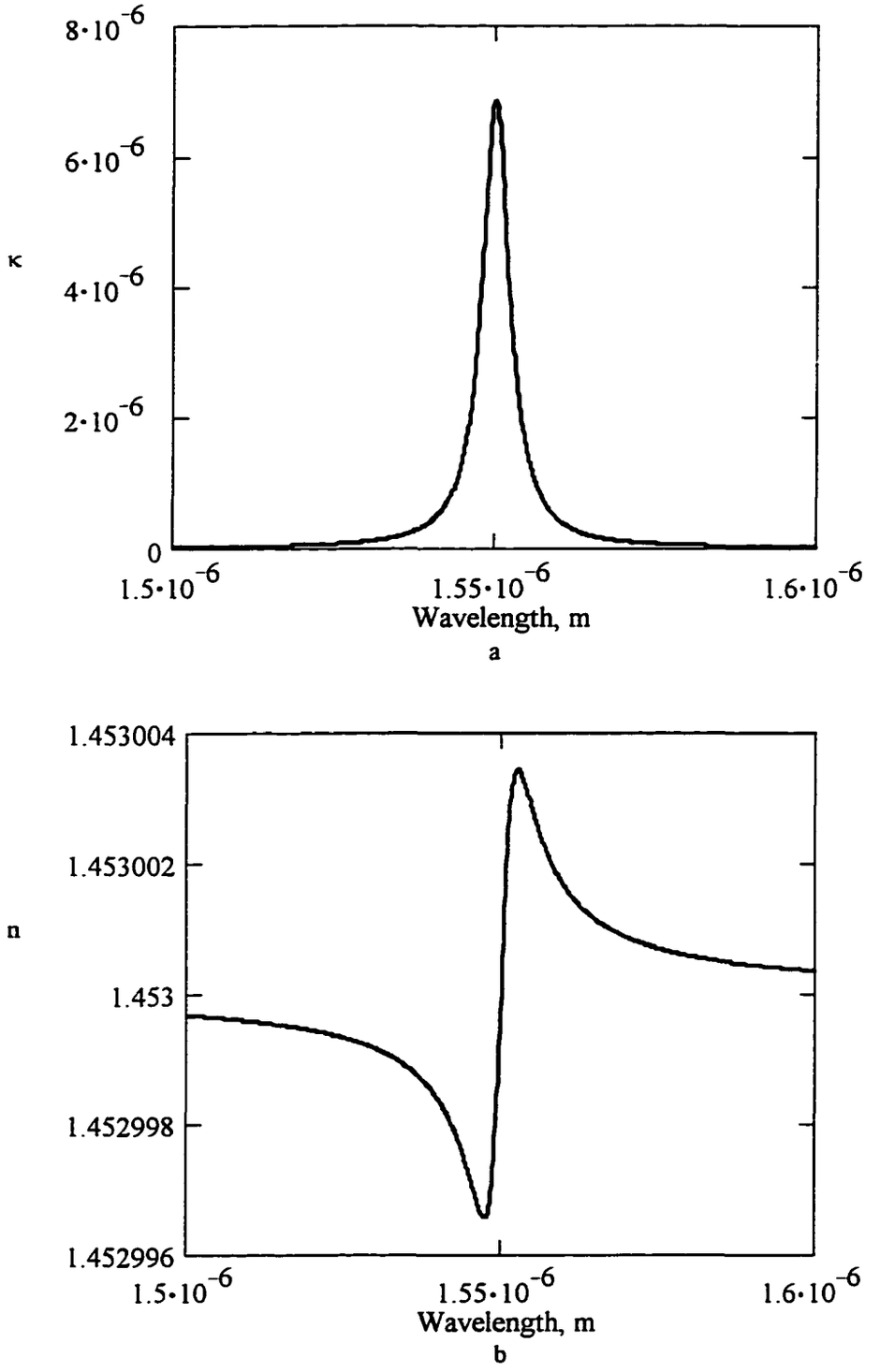

Figure 4: Variation of a) κ and b) n with wavelength for dense medium. For these curves, λ_o = 1550 nm, $N = 3*10^{19}$ m^{-3}, and $\Delta\lambda$ = 1 nm.

2.2 Theory of Wave Propagation in Fiber Optic Couplers

In this section, the theory of fiber optic coupler (FOC) is presented. FOC's have distinct waveguiding properties that are highly dependent on the refractive index of the medium surrounding the coupler.

The 2 x 2 coupler has the simplest structure for single mode operation, as shown in Figure 5. It has two input ports, P_1 and P_2, and two output ports, P_3 and P_4. Several models have been proposed to explain the coupling at the fused region. A simple model was proposed by Payne et al. [12] where the fused region is approximated as a rectangle with length 2a and width a, as shown in Figure 6. During fabrication, the core diameter will be reduced to a negligibly small radius; therefore, all guided modes will appear in the cladding, which forms the new core in the fused region. Waveguiding can still occur due to the composite structure of the cladding and its surrounding medium. It has been shown that power exchange in a coupler occurs by the beating of the two lowest-order cladding modes of the composite structure [13-15]. By using the propagation constants for these low-order modes, the coupling coefficient describing the strength of interaction

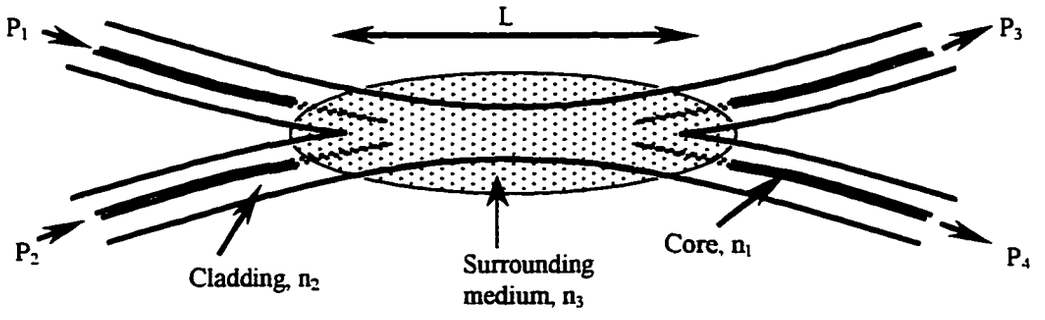

Figure 5: Schematic of a fiber optic coupler.

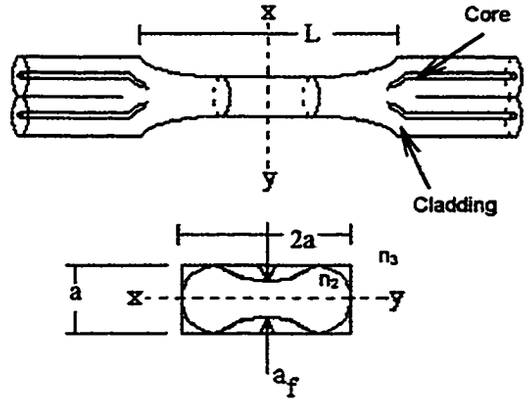

Figure 6: Approximate shape of a fused taper coupler using a rectangular cross-section for the fused region.

between these modes could be expressed as [12]

$$C = \frac{3\pi\lambda}{32 n_2 a^2} \frac{1}{(1+\frac{1}{V})^2} \tag{27}$$

where a is the width of the modeled rectangle, λ is the wavelength, n_2 is the index of refraction of the clad and

$$V = ak(n_2^2 - n_3^2)^{\frac{1}{2}}. \tag{28}$$

n_3 is the index of refraction of the medium surrounding the coupling region. Equation 27 is very useful in determining the effect of n_3, a, and V on the output of the coupler. More importantly, the power P_3 and P_4 at the output ports of the coupler are

$$P_3 = P_1 \sin^2(CL) \tag{29}$$

$$P_4 = P_1 \cos^2(CL) \tag{30}$$

where P_1 is the input power and L is the length of the coupler region. Hence, the effect of L can also be examined, as shown in Figure 7. Keeping the coupling coefficient fixed, as

the length of the coupler is increased, the period of the sinusoidal variations in the spectral output decreases.

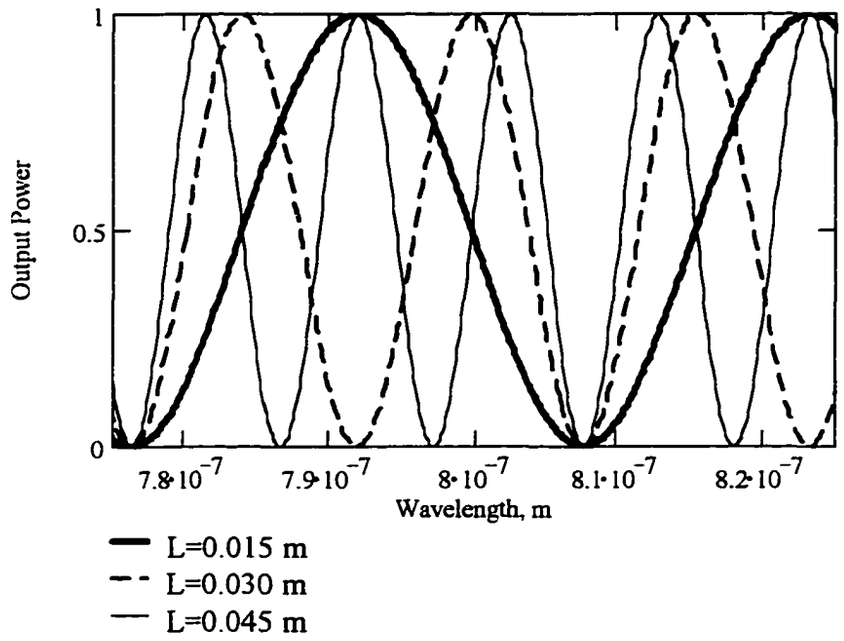

Figure 7: Variation of output power P_3 for different values of the coupler length L. $n_2 = 1.458$, $n_3 = 1$, and $a = 5.25$ μm.

Payne et al. [16] show that it is possible to incorporate polarization effects in the above model. It was noticed that long couplers (i.e. large L values) exhibited a modulation of the amplitudes of the power splitting ratio as a function of wavelength. The model used was that of a rectangle for strongly fused coupled regions and two touching cylinders for weakly fused coupled regions, as shown in Figure 8 [16]. The output power P at one of the output ports of the coupler is described as

$$P = \frac{1}{2}\{1 + \cos[(C_x + C_y)L]\cos[(C_x - C_y)L]\} \tag{31}$$

where C_x and C_y are the coupling strengths of the x- and y-polarization, respectively, P_1 = 1, and

$$C_x + C_y = \frac{3\pi\lambda}{32 n_2 a^2}\left[\frac{1}{\left(1+\frac{1}{V}\right)^2} + \frac{1}{\left(1+\frac{n_3^2}{n_2^2}\cdot\frac{1}{V}\right)^2}\right] \tag{32}$$

$$C_x - C_y = \frac{3\pi\lambda}{16 n_2 a^2}\cdot\frac{1}{V}\left(1-\frac{n_3^2}{n_2^2}\right) \tag{33}$$

for strongly fused couplers and

$$C_x + C_y = \frac{2^{\frac{7}{2}}\left(n_2^2 - n_3^2\right)^{\frac{1}{2}} U_\infty^2}{n_2 a \pi^{\frac{1}{2}} V^{\frac{5}{2}}} \tag{34}$$

$$C_x - C_y = \frac{2^{\frac{5}{2}}\left(n_2^2 - n_3^2\right)^{\frac{1}{2}} U_\infty^2}{n_2^3 a \pi^{\frac{1}{2}} V^{\frac{7}{2}}} \tag{35}$$

for weakly fused couplers, where $U_\infty = 2.405$ [16].

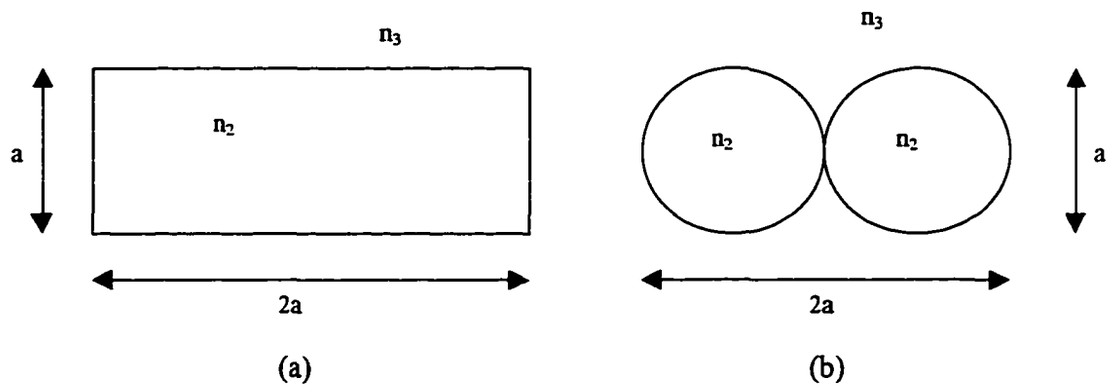

Figure 8: Approximations used to model the fused coupled region of (a) a strongly fused coupler and (b) a weakly fused coupler.

It is obvious that the cross-sectional shape of the fused region is important in deriving the coupling coefficient, and hence the output port power. Snyder and Zheng [17], in their interest to include polarization effects in the above model, derived the coupling coefficients C_x and C_y for several cross-sectional shapes, including the rectangle and the ellipse. Both cross-sections model the fused coupler very well. However, the elliptical cross-section includes the polarization beam splitting property, and hence is more accurate for modeling polarization effects [17-19]. In this research, however, polarization effects are ignored to make the analysis easier. Therefore, the fiber optic coupler fused region is modeled using the rectangle model.

Equations 27-30 show that the output of a fiber optic coupler modeled using a simple rectangular cross-section for the fused region is dependent on the refractive index of the cladding and the medium surrounding the fused region of the fiber optic coupler. In addition, these outputs are dependent on the physical parameters on the fiber optic coupler, namely the waist diameter and the length of the coupler. Keeping all parameters fixed, it is found that as the waist diameter is increased, the period of the spectral oscillations increases, as shown in Figure 9. If the refractive index of the surrounding medium is increased from $n_3 = 1.00$ to $n_3 = 1.450$ while keeping all other parameters constant, it is also found that the period of the spectral oscillations increases, as shown in Figure 10. Finally, if the external medium is air and the cladding refractive index is decreased from 1.458 to 1.333, the period of the spectral oscillations increases, as shown in Figure 11.

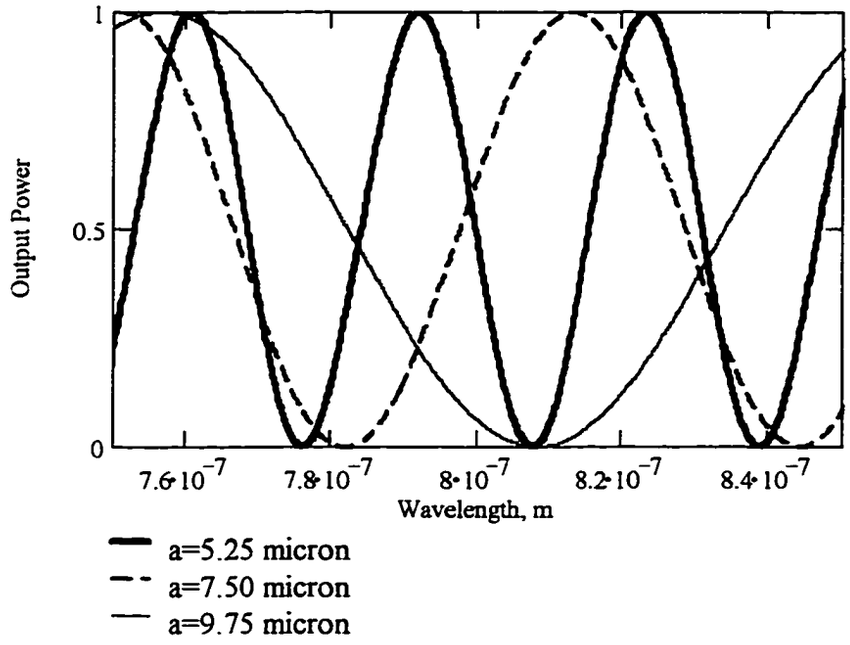

Figure 9: Variation of output power P_3 for different values of waist diameter a. $n_2 = 1.458$, $n_3 = 1$, and L = 0.015 m.

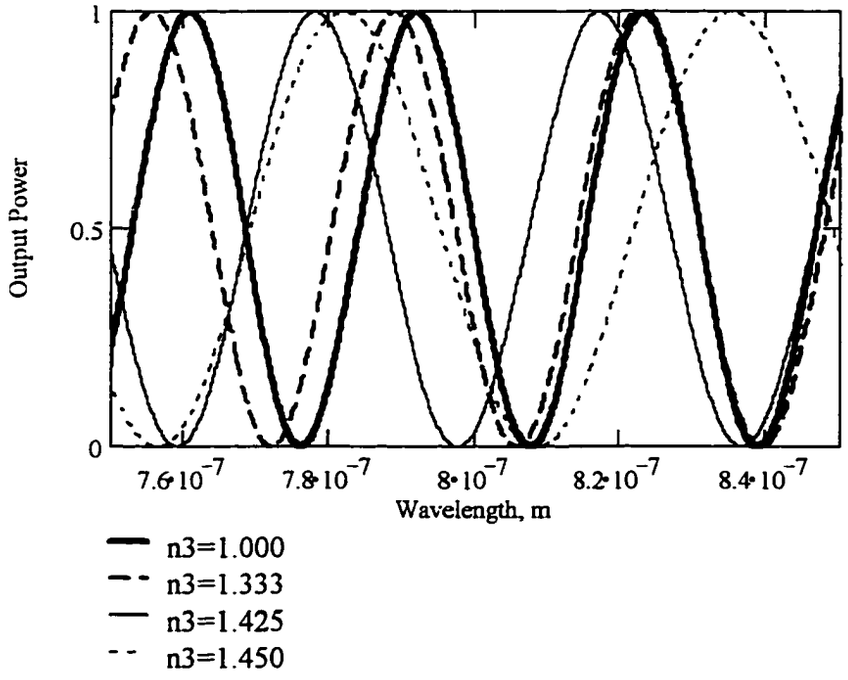

Figure 10: Variation of output power P_3 for different values of external refractive index n_3. $n_2 = 1.458$, L = 0.015 m, and a = 5.25 μm.

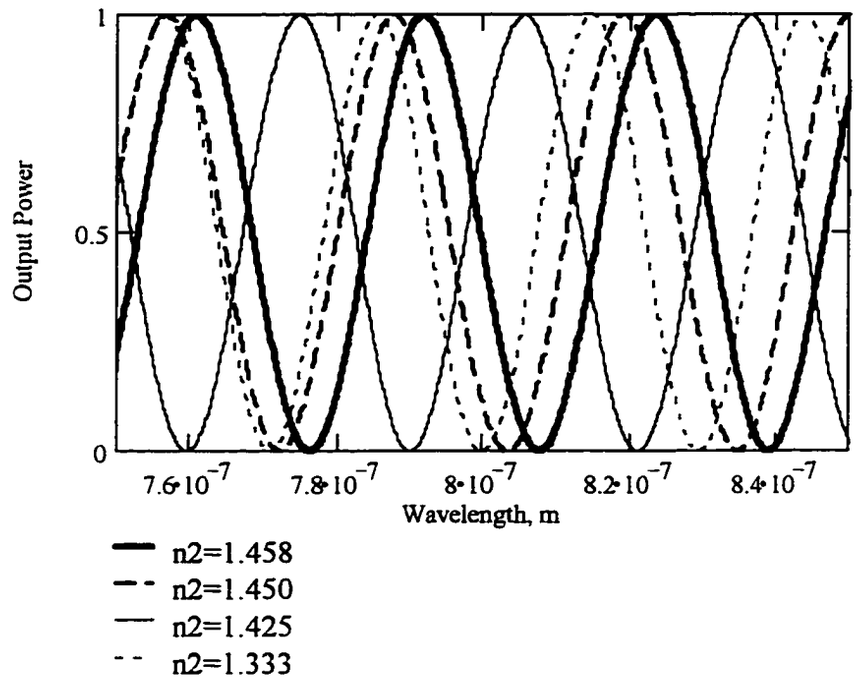

Figure 11: Variation of output power P_3 for different values of cladding refractive index n_2. L = 0.015 m, n_3 = 1, and a = 5.25 μm.

2.3 Theory of Wave Propagation in Fiber Optic Tapers

The fiber optic taper (FOT) is a much simpler structure than the coupler. A FOT is thought of as the basic element for understanding fiber optic couplers. The spectral output of FOT is oscillatory with wavelength, hence, devices such as power splitters, wavelength division multiplexers, and wavelength and mode filters have been fabricated from these structures to take advantage of the unique output [20-27]. FOT's are made similarly to fiber optic couplers. A schematic of a fiber optic taper is shown in Figure 12. A taper has three distinct regions. For a single mode fiber, power transfer from HE_{11} mode to other modes occurs within Regions 1 and 3 where the diameter changes drastically. During fabrication, the output will be oscillatory depending on the taper

length and waist diameter. After fabrication, the spectral output is oscillatory with wavelength [28]. The general theoretical expressions describing the oscillatory output of a taper are given as [29, 30]

$$P_j = \left(\frac{C_{jl}(z)}{\delta\beta(n_e)}\right)^2 + \left(\frac{C_{jl}(0)}{\delta\beta(n_e)}\right)^2 - 2\left(\frac{C_{jl}(z)}{\delta\beta(n_e)}\right)^2\left(\frac{C_{jl}(0)}{\delta\beta(n_e)}\right)^2 \cos\left(\overline{\delta\beta(n_e)}\cdot z\right) \quad (36)$$

where P_j is the power coupled from the l^{th} mode to the j^{th} mode and $\overline{\delta\beta(n_e)}$ is the accumulated phase difference between the modes. This is given by

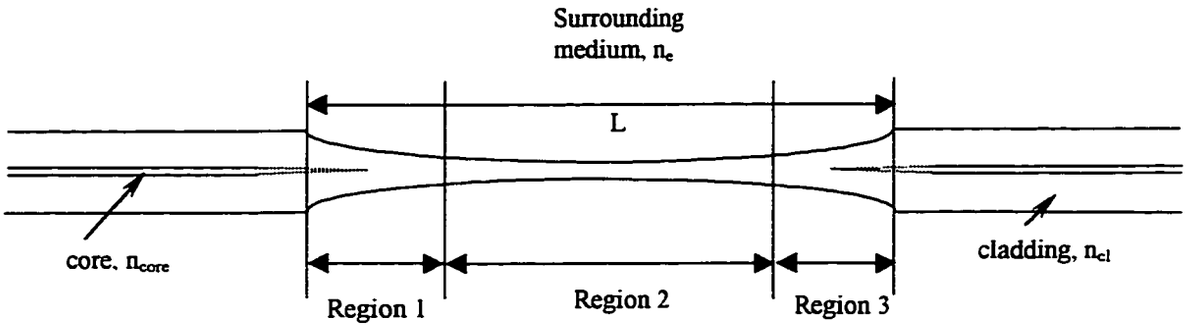

Figure 12: A schematic of a biconical taper profile.

$$\overline{\delta\beta(n_e)} = \frac{1}{L}\int_0^L \{\beta_1(z, n_e) \mp \beta_j(z, n_e)\}dz$$

$$\beta_1(z, n_e) = \frac{1}{\rho_z}\left\{\frac{V_1^2}{2\Delta} - U_1^2\right\}^{\frac{1}{2}}$$

$$\beta_j(z, n_e) = \frac{1}{\rho_z}\left\{\frac{V_j^2}{2\Delta} - U_j^2\right\}^{\frac{1}{2}} \quad (37)$$

$$\Delta = \frac{n_{cl}^2 - n_e^2}{2n_{cl}^2}$$

where L is the length of the taper, n_e is the refractive index of the surrounding medium, and U and V are waveguide parameters. Equations 36 and 37 show that the phase term of the oscillatory output of the taper depends not only on the wavelength, but also on the

refractive index of the external medium. In the above equations, the core refractive index is replaced by that of the cladding since the core disappears in the tapered region. In Region 2, any change in n_e will contribute to a phase shift in the oscillatory output. It is evident that the output of a taper is extremely sensitive to the refractive index of the external medium.

2.4 Theory of Evanescent Wave Absorption in Optical Fibers

Conventional absorption spectroscopy involves sending light through a sample media and measuring the intensity of detected light as a function of wavelength. By tuning the wavelength of light incident on the sample, one can sweep across wavelength and determine where, if any, the sample begins to absorb light. The concentration of the species is expressed by the Beer-Lambert's law [31], namely

$$A = \log\left(\frac{P_o}{P}\right) = \boldsymbol{abc} \tag{38}$$

where A is the absorbance of the sample, P_o is the incident intensity, P is the transmitted intensity, $\boldsymbol{a}$ is the absorptivity of the sample at a particular wavelength, $\boldsymbol{b}$ is the path length the light traverses through the sample, and $\boldsymbol{c}$ is the concentration of the sample.

An extension of conventional absorption is evanescent wave absorption spectroscopy. This technique is based on the phenomenon of attenuated total reflection (ATR) of light from a dielectric medium, which impinges onto an absorbing medium of a lower refractive index [6]. Recently [32], fiber optics have been used instead of conventional ATR elements such as ZnSe because of convenience of handling, easy sample loading, and low cost. In an optical fiber, light propagates both in the core and in the cladding. When light is incident at the interface of two optically transparent regions

with high (n_1) and low (n_2) indices of refraction, total internal reflection (TIR) occurs for angles of incidence greater than a critical angle $\theta > \theta_c$, where

$$\sin\theta_c = \frac{n_2}{n_1}. \tag{39}$$

At the interface, the phase of the light will change on reflection, resulting in a finite standing wave amplitude. From Maxwell's equations, this results in an exponentially decaying standing wave away from the interface into the region n_2. The 'penetration depth' d_p of this decaying exponential standing wave into n_2 is defined as

$$d_p = \frac{\lambda}{2\pi n_1\left(\sin^2\theta - \sin^2\theta_c\right)^{\frac{1}{2}}} \tag{40}$$

where λ is the wavelength of light incident on the interface. d_p has a minimum value for $\theta = 90°$. At θ_c, $d_p \rightarrow \infty$. Hence, bringing a light-absorbing medium within the field region where the decaying exponential standing wave is appreciable can produce attenuation of the reflected energy.

This evanescent wave absorption technique can also be applied using an optical fiber. The fiber transmittance can be given as [33]

$$P = P_o\exp\left(-\alpha_{eff}L\right) \tag{41}$$

where α_{eff} is the absorption coefficient due to evanescent wave absorption on the fiber and L is the interaction length.

Several research groups have recently derived analytical forms of the effective evanescent wave absorption coefficient using a fiber. One derivation is given by Messica, Greenstein, and Katzir [34]. Their model accounts for various launching angles,

Fresnel transmission and reflection from the input and output fiber faces, and bulk and evanescent wave absorption. The transmission function was derived as

$$T = \frac{t^4 \left[r_{ATR}^2\right]^N \exp\left(-\alpha_{co} L_p\right)}{M} \tag{42}$$

where t^2 is the Fresnel power transmission coefficient, and M is the contribution due to multiple reflections from the fiber end faces. The particular form of the contribution of the evanescent wave absorption on the transmission is given as

$$\left[r_{ATR}^2\right]^N = \left[\frac{1}{2}\left(r_s^2 + r_p^2\right)\right]^N \tag{43}$$

where r_s and r_p are the Fresnel reflection coefficients for s- and p-polarization and are defined as follows:

$$r_s^2 = 1 - \frac{4 n_{co} n_{cl}^2 \cos\psi \left(\frac{\kappa_{cl}}{n_{cl}} - \frac{\kappa_{co}}{n_{co}}\right)}{\left(n_{co}^2 - n_{cl}^2\right)\left(n_{co}^2 \sin^2\psi - n_{cl}^2\right)^{\frac{1}{2}}} \tag{44}$$

$$r_p^2 = 1 - \frac{4 n_{co}^2 n_{cl}^2 \cos\psi \left(\frac{\kappa_{cl}}{n_{cl}} - \frac{\kappa_{co}}{n_{co}}\right) \times \left(2 n_{co}^2 \sin^2\psi - n_{cl}^2\right)}{\left(n_{co}^2 - n_{cl}^2\right)\left(n_{co}^2 \sin^2\psi - n_{cl}^2\right)^{\frac{1}{2}} \times \left(n_{co}^2 \sin^2\psi - n_{cl}^2 \cos^2\psi\right)} \tag{45}$$

where $\cos\psi = \sin\theta \cos\gamma_{skew}$, $\kappa_i = \alpha_i \lambda / 4\pi$ such that i stands for the core or the clad, γ_{skew} is the skewness angle of the propagating wave, and α is the standard absorption coefficient. N is the number of reflections the propagating light makes at the interface. The right hand side of Equation 42 replaces the exponential term in Equation 41, giving the evanescent wave absorption a complicated dependence on wavelength, refractive indices and extinction coefficients. This is different from conventional absorption

spectroscopy where the Beer-Lambert law is normally obeyed. However, this analysis of the transmission based on the theoretical model shows that the evanescent wave absorption follows a pseudo-Beer-Lambert dependence on fiber length. Also, the absorption is inversely proportional to the fiber radius and has a parabolic dependence on the coupling angle.

Another formulation of the evanescent wave absorption coefficient looks at the launching conditions of the light into the fiber. This analysis is based on the expression [29]

$$\alpha = NT \tag{46}$$

where N is the number of ray reflections per unit length in the fiber core and T is the Fresnel transmission coefficient at the interface. If the core has a radius of a, the cladding has a refractive index of n_2, and the complex refractive index of the absorbing medium is $(n_3 - i\kappa_3)$, then

$$N = \frac{\cot\theta}{2a} \tag{47}$$

$$T = \frac{\alpha\lambda n_3 \cos\theta}{\pi\left(n_2^2 - n_3^2\right)\left[\sin^2\theta - \left(\frac{n_3}{n_2}\right)^2\right]^{\frac{1}{2}}}. \tag{48}$$

Hence, the evanescent wave absorption coefficient for a ray making an angle θ with the normal to the interface is [35-37]

$$\alpha(\theta) = \frac{\alpha\lambda n_3 \cos^2\theta}{2\pi a\left(n_2^2 - n_3^2\right)\sin\theta\left[\sin^2\theta - \left(\frac{n_3}{n_2}\right)^2\right]^{\frac{1}{2}}}. \tag{49}$$

However, when multiple rays are launched into the fiber over a range of angles (θ_1, θ_2), the power distribution must be integrated over the range of incident angles to obtain an effective evanescent wave absorption coefficient [36-37]:

$$\alpha_{\text{eff}}(\theta_1,\theta_2)=\frac{\int_{\theta_1}^{\theta_2}\sin\theta\cos\theta\alpha(\theta)d\theta}{\int_{\theta_1}^{\theta_2}\sin\theta\cos\theta d\theta}. \tag{50}$$

Equation 50 can be evaluated for a fiber with a uniform core (i.e. a is constant) by substituting Equation 49 into 50 and integrating the numerator and denominator, yielding [36-37]

$$\alpha_{\text{eff}}=\frac{\alpha\lambda n_2}{\pi\rho\left(n_2^2-n_3^2\right)}\frac{f(\theta_2)-f(\theta_1)}{\sin^2\theta_2-\sin^2\theta_1}$$

$$f(\theta)=\frac{1}{2\left(\frac{n_2}{n_3}\right)^3}\left\{\left(2\left(\frac{n_2}{n_3}\right)^2-1\right)\ln\left[2\left(q^2-1\right)^{\frac{1}{2}}+2q\right]-q\left(q^2-1\right)^{\frac{1}{2}}\right\} \tag{51}$$

$$q=\frac{n_2}{n_3}\sin\theta$$

where $\theta_1=\sin^{-1}(n_2/n_1)$ and $\theta_2=90°$. Equations 51 can be substituted into Equation 41 to obtain the power output of an optical fiber subjected to evanescent wave absorption. To increase the sensitivity, the penetration depth should be increased by launching the light into the fiber at an angle near θ_c. Figure 13 shows that as the incident angle of the light approaches the critical angle, the evanescent wave extends further into the surrounding medium. The incident wavelength also plays a role in the sensitivity of evanescent wave

absorption. Figure 13 shows that longer wavelengths produce a larger penetration depth into the surrounding medium for the same incident angles.

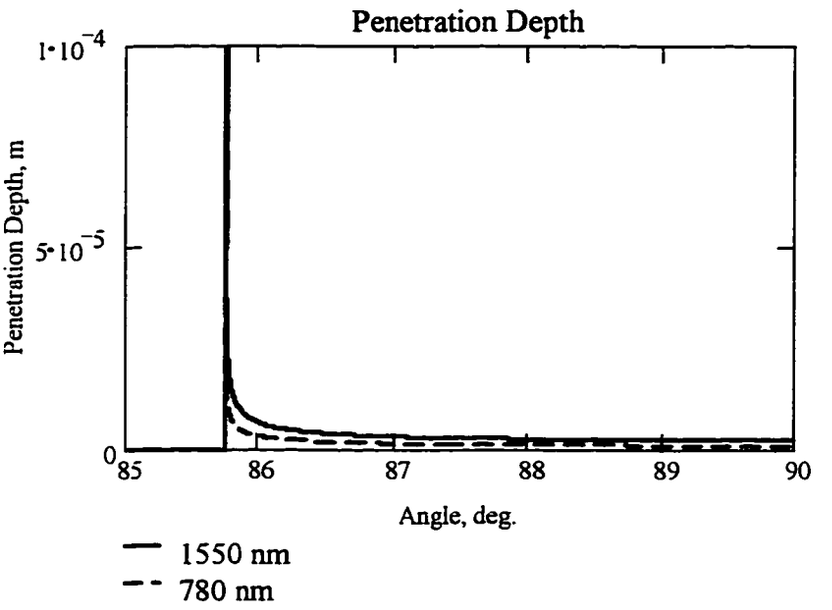

Figure 13: The penetration depth of the evanescent wave increases as the incident angle approaches the critical angle. Longer wavelengths will also produce a larger penetration depth. $n_1 = 1.462$ and $n_2 = 1.458$. $\theta_c = 85.76°$.

Figure 14 shows the variation of the penetration depth of the evanescent wave as a function of incident angle for various refractive indices of the surrounding medium. As the surrounding index of refraction n_2 approaches that of the high refractive index medium n_1, the critical angle increases, limiting the range of incident angles at which the penetration depth is large enough to produce evanescent wave absorption by the surrounding medium.

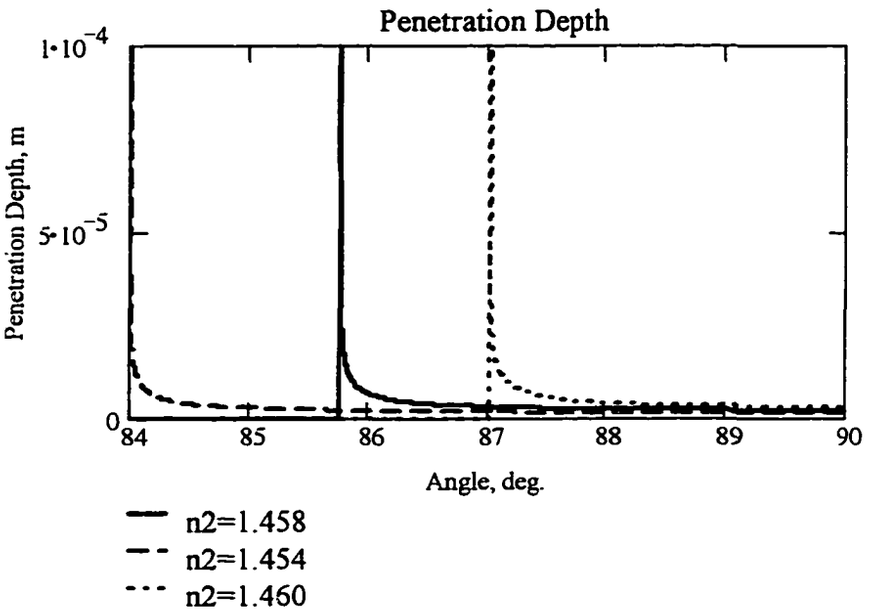

Figure 14: Penetration depth of the evanescent wave as a function of incident angle for various refractive indices for the external medium.

The sensitivity of evanescent wave absorption can be enhanced by decreasing the radius of the sensing fiber, which increases the number of reflections at the interface of the absorbing media. Figure 15 shows that as the fiber core radius is decreased, the effective absorption coefficient increases at the absorption wavelength peak. A longer interaction length of the fiber will also increase the evanescent wave absorption, as shown in Figure 16.

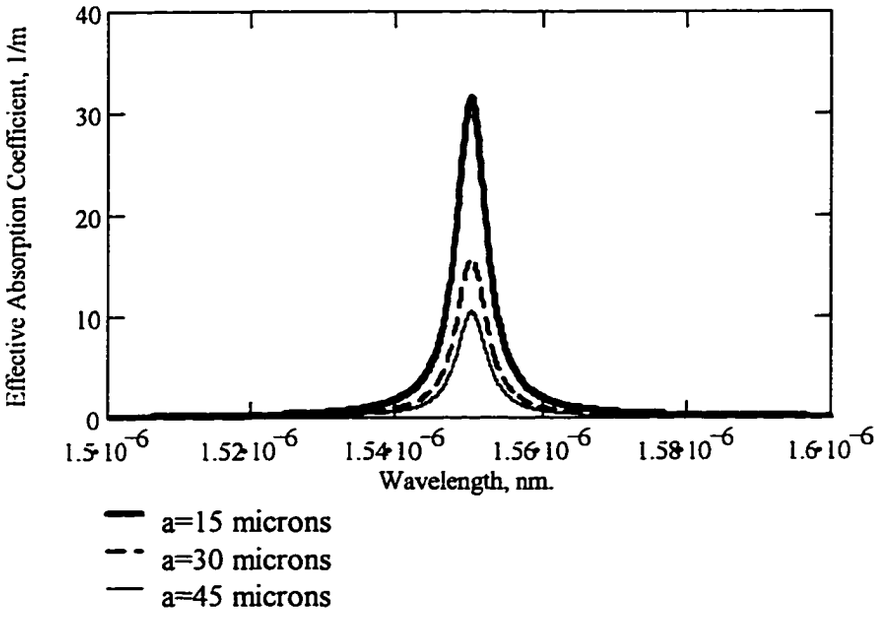

Figure 15: Effect of core radius on the effective absorption coefficient. Parameters: $N = 10^{21}$ m^{-3}, n_1 = 1.462, n_2 = 1.458, n_3 = 1.453, L = 0.0285 m, $\Delta\lambda$ = 5 nm.

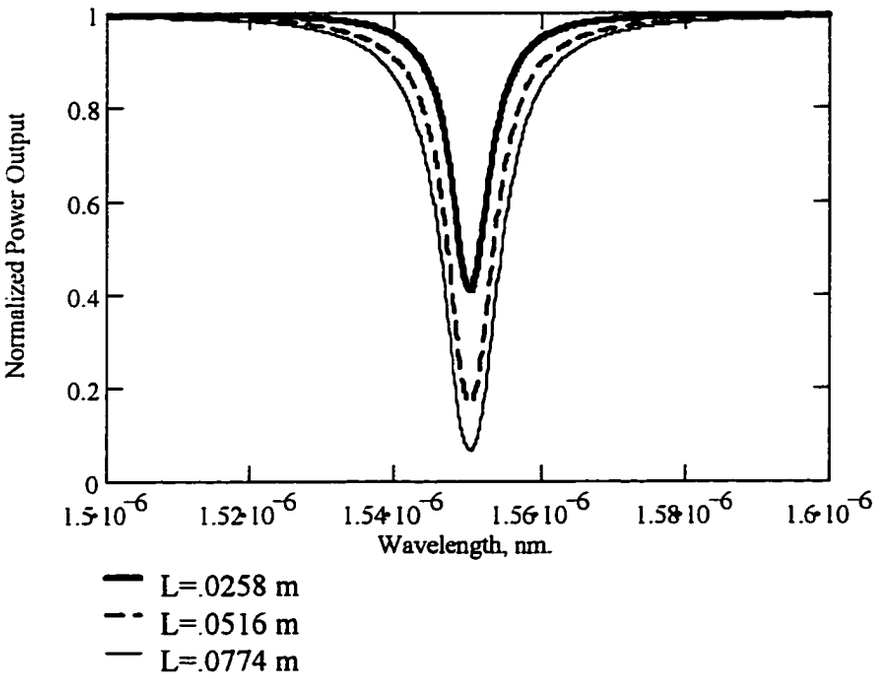

Figure 16: Effect of length of fiber on the spectral output of evanescent wave absorption sensor. Parameters: $N = 10^{21}$ m^{-3}, n_1 = 1.462, n_2 = 1.458, n_3 = 1.453, a = 15 μm, $\Delta\lambda$ = 5 nm.

2.5 Kramers-Kronig Effect on Fiber Optic Couplers and Tapers

Because the spectral output of FOC's and FOT's is extremely sensitive to the refractive index of the external medium surrounding them, we can examine the effect of Kramers-Kronig anomalous dispersion due to evanescent wave absorption. Combining these effects, the output power from a FOC can be given by

$$P_3(\lambda) = P_o \sin^2[C(\lambda)L]\exp[-\alpha_{co}(\lambda)L]\exp[-\alpha_{eff}(\lambda)L] \quad (52)$$

$$P_4(\lambda) = P_o \cos^2[C(\lambda)L]\exp[-\alpha_{co}(\lambda)L]\exp[-\alpha_{eff}(\lambda)L] \quad (53)$$

where $\alpha_{co}(\lambda)$ is the intrinsic absorption due to the optical fiber and $\alpha_{eff}(\lambda)$ is the effective evanescent wave absorption coefficient.

It was shown that the presence of anomalous dispersion due to the Kramers-Kronig effect must be accompanied by the presence of an absorption band, and vice versa. However, the power output derived for FOC's and FOT's assume that no absorption occurs in the medium surrounding the fused or tapered region of the structure. Equations 29, 30, and 36 must be modified to account for absorption due to the presence of an absorbing species.

From Section II.1, the presence of an absorption peak indicates the presence of anomalous dispersion in the refractive index, as given by the Kramers-Kronig effect. Thus, if an absorbing species is present in the fused region of a fiber optic coupler, then two simultaneous effects will occur. First, light propagating the coupler will undergo evanescent wave absorption. Second, light will couple from one fiber to another due to the change in refractive index caused by the Kramers-Kronig effect. To see these effects, consider an absorption line of the external medium at λ_o = 1550 nm with full-width half-maximum $\Delta\lambda = 5\text{nm}$ and a density N = 10^{21} atoms·m^{-3}. The absorbing medium has a

nominal refractive index n_3 = 1.453. The fiber optic coupler has the following parameters: L = 28.5 mm, ρ = 15 μm, and clad index n_2 = 1.458. A plot of the refractive index and extinction coefficient as a function of wavelength is shown in Figure 17 a and b. Assuming that the fiber is lossless (i.e. $\alpha_{co} = 0$) the spectral response of the fiber optic coupler in air (dotted line) and in a lossless medium of refractive index n_3 = 1.453 (solid line) is shown in Figure 18. When the fiber optic coupler is placed in the absorbing medium, the V-parameter (Equation 28) and the coupling coefficient C (Equation 27) show a perturbation in the otherwise smooth curves, as show in Figures 19 and 20, respectively. The corresponding fiber optic evanescent wave absorption due to the presence of anomalous dispersion shown in Figure 17 is shown in Figure 21. Combining all the effects on the fiber optic coupler, the spectral output will show a change in output power where the refractive index has anomalous dispersion. The spectral output will also show a decrease in intensity near the absorption band due to the evanescent wave absorption of light in the fused region of the coupler. Both complementary outputs of the coupler are shown in Figure 22. The output curves include dispersion and absorption effects. Note that while absorption produces the same loss in both outputs, dispersion produces shifts in the curves opposite to each other by virtue of the complementary trigonometric functions in Equations 52 and 53. Therefore the difference over sum of the outputs, $\frac{(P_3 - P_4)}{(P_3 + P_4)}$, eliminates the common mode absorption and other losses associated with coupler and gives the output due to dispersion alone. This is shown as curve 3 in Figure 23, where curves 1 and 2 are the same curves shown in Figure 22 and are given for reference. Within the linear region, the output has a maximum and a minimum near

the resonance wavelength similar to the dispersion of n_3. It is different from the normal oscillations of the coupler output and is clearly distinguishable. This change in output ΔP around the absorption peak is dependent on Δn.

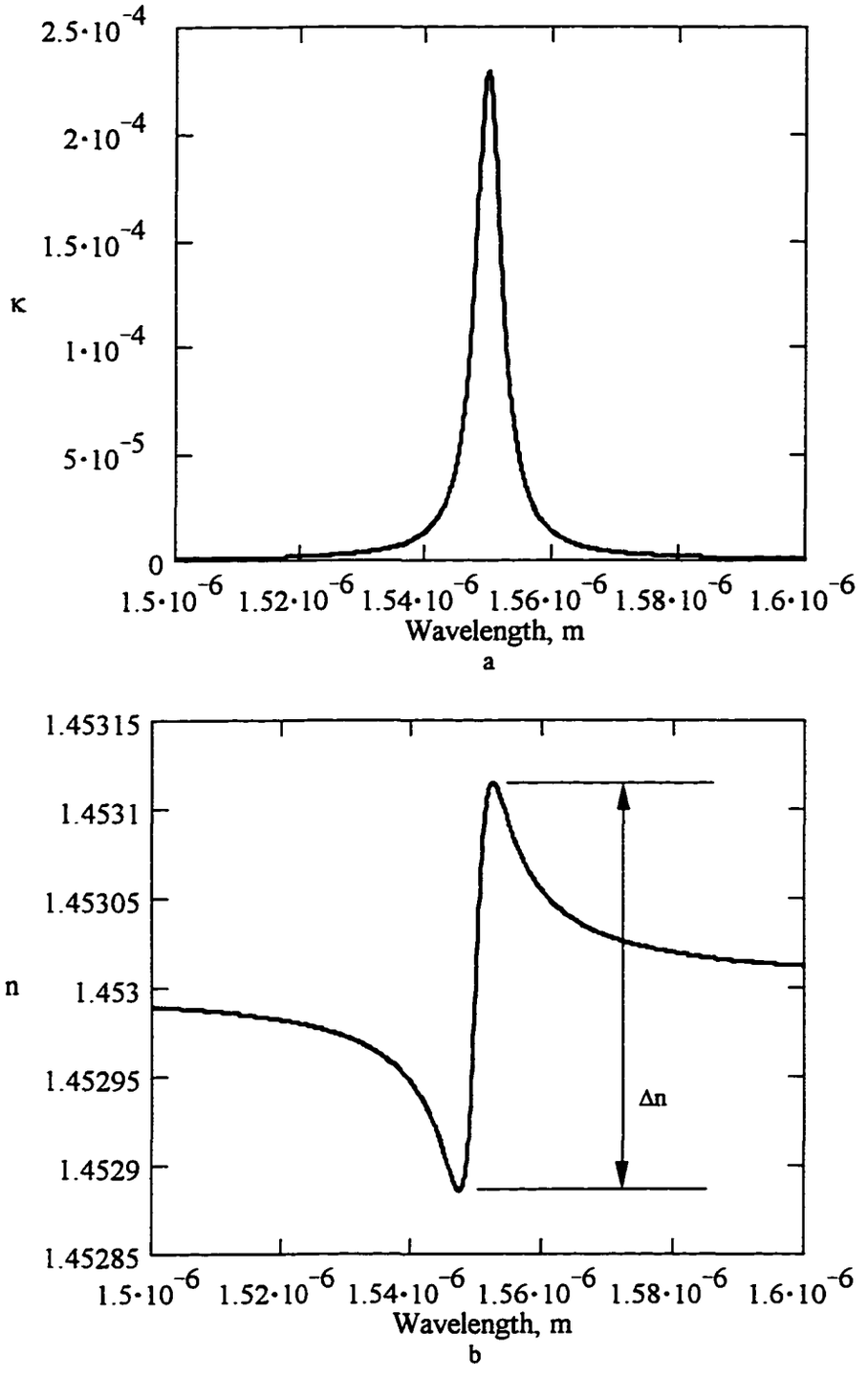

Figure 17: Variation of a) κ and b) n with wavelength. For these curves, λ_o = 1550 nm, N = $1*10^{21}$ m^3. and $\Delta\lambda$ = 5 nm.

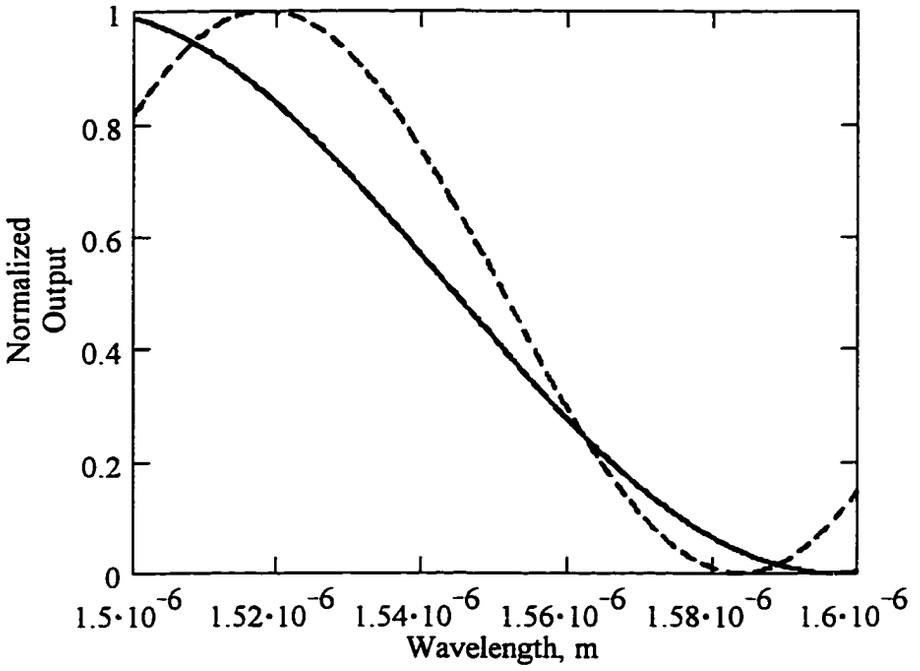

Figure 18: The spectral response of the fiber optic coupler in air (dotted line) and in a lossless medium (solid line) of refractive index $n_3 = 1.453$.

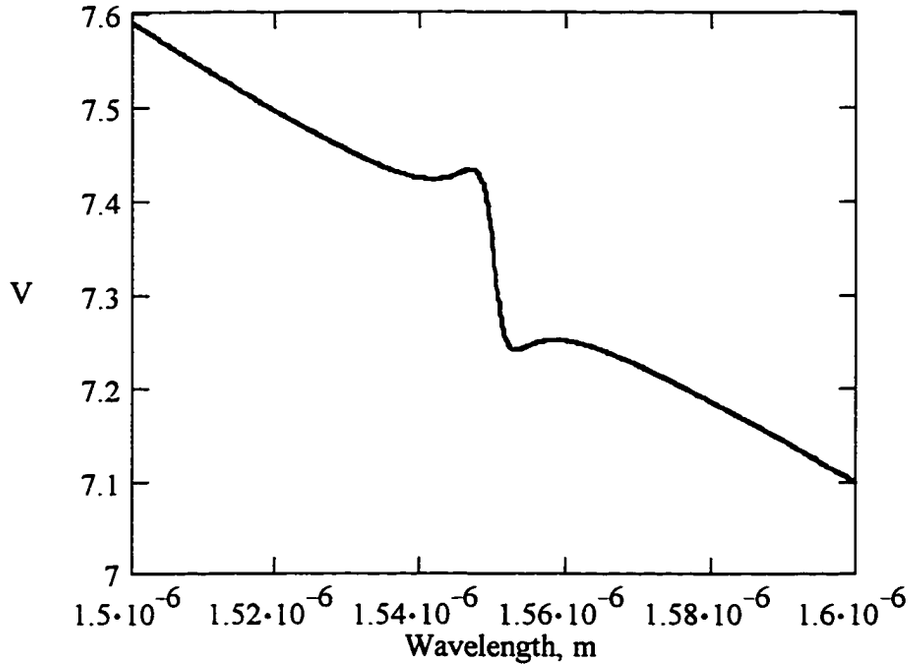

Figure 19: Variation of the V-parameter for a fiber optic coupler immersed in an absorbing medium. $N = 10^{21}$ m^{-3}, $\Delta\lambda = 5$ nm, $\alpha(1550\text{ nm}) = 1.857$ cm^{-1}.

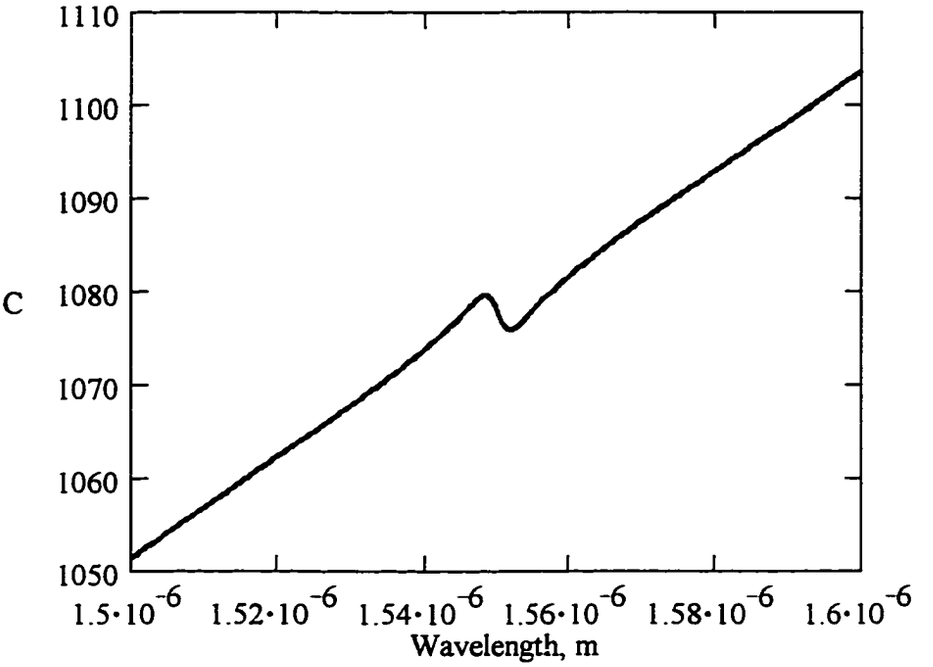

Figure 20: Variation of the coupling coefficient C for a fiber optic coupler immersed in an absorbing medium.

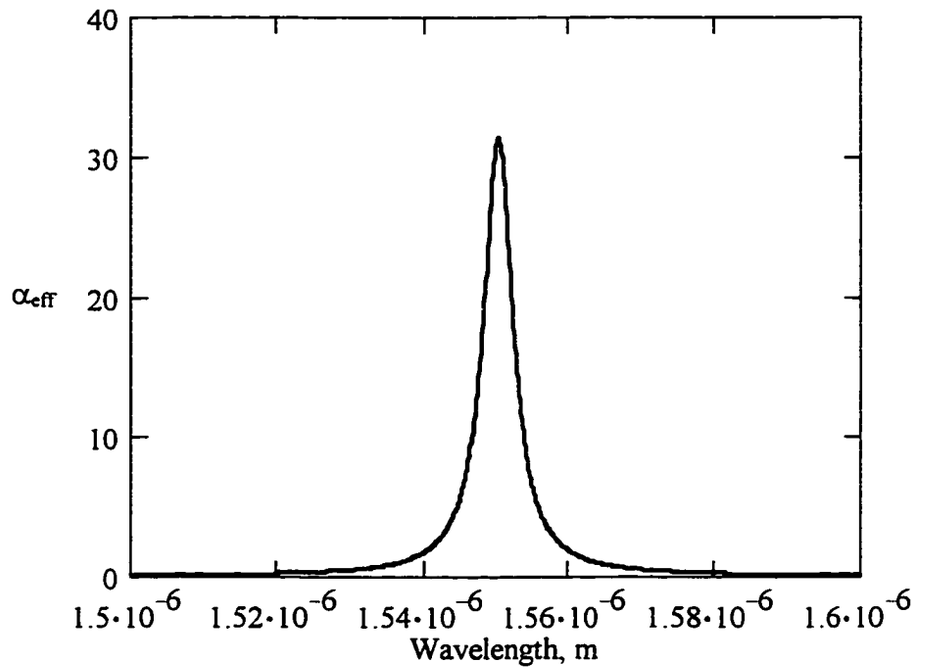

Figure 21: Evanescent wave absorption in a fiber optic coupler due to the presence of anomalous dispersion.

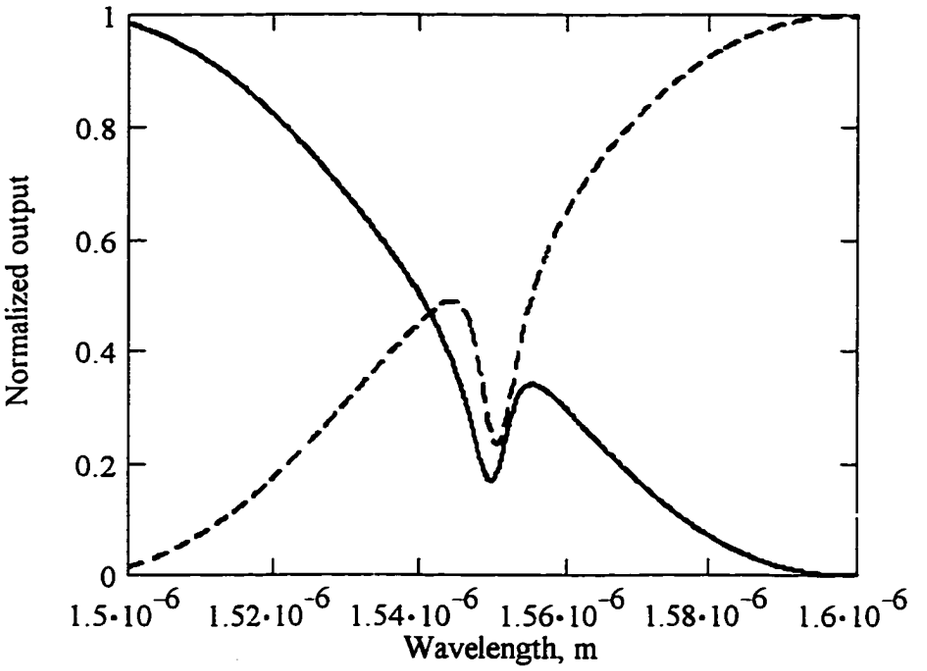

Figure 22: Complementary outputs of a fiber optic coupler immersed in an absorbing medium. These curves show the combined effect of anomalous dispersion and evanescent wave absorption.

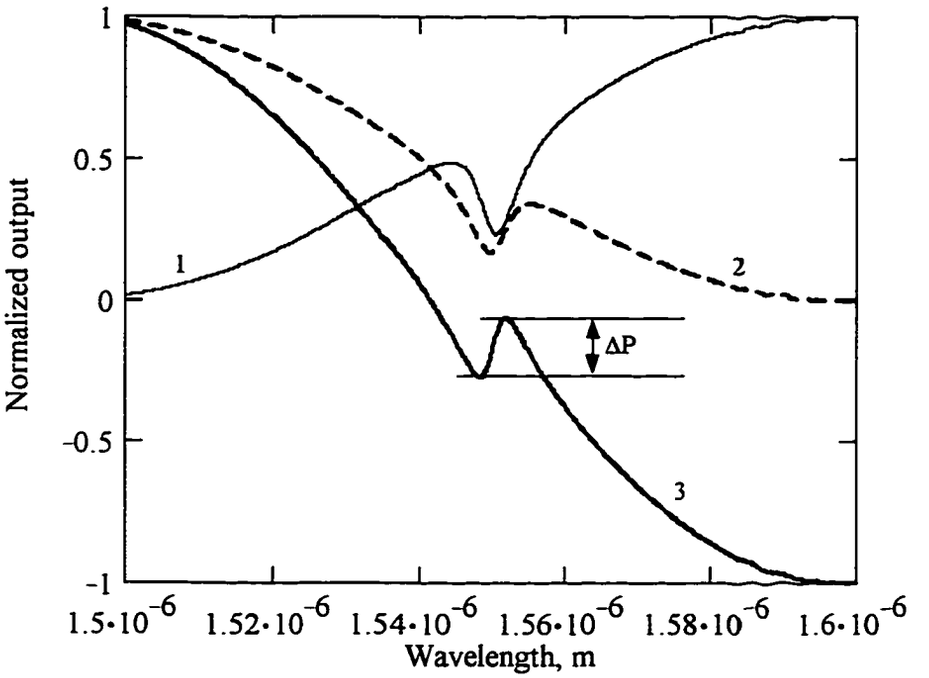

Figure 23: Curves 1 and 2- Complementary output P_3 and P_4. These curves are repeated from Figure 14 for comparison with Curve 3. Curve 3- Difference over sum showing the effect of normal and anomalous dispersion only.

CHAPTER III

EXPERIMENTAL METHODS

Theoretical modeling has shown that the output of fiber optic couplers and tapers will be affected by normal and anomalous dispersion. In this chapter, experimental details are presented to verify this effect. This chapter also provides details of fabrication of fused couplers and tapers and measurement of their output characteristics. The preparation of suitable dye solutions and the measurement of their transmission characteristics are given.

3.1 Fiber Optic Coupler and Taper Fabrication

Fiber optic couplers and tapers were fabricated using the fuse and pull method. A compact microfurnace provided the heating required to bring the fiber to its softening temperature so that fusing and tapering of the fibers could be accomplished. The microfurnace has a maximum working temperature of 1450° C. The opening of the microfurnace is approximately five centimeters long with a 0.5-cm wide slit, which allows the fiber to be placed within the heating zone of the furnace. The microfurnace is mounted on an x-axis translation stage and set on an optical rail to allow for alignment in the x- and y-directions. A second optical rail is placed perpendicular to the first rail such that the microfurnace slit opening is parallel to the second rail. This allows rail mounts to be placed on the second rail so that the fibers can be held while the fusing and tapering process is being conducted.

Corning Flexcor 780 single mode fiber was used to fabricate the fiber optic couplers. This fiber has a core diameter of 5 μm and a cladding diameter of 125 μm. The

cutoff wavelength is 720 ± 50 nm. The core refractive index is 1.460257 and the clad refractive index is 1.449180, as specified at 1550 nm by the manufacturer. The fiber optic couplers were fabricated using the fuse and pull method. Approximately 5 cm of the acrylate buffer coating was stripped off from two fibers using dichloromethane and cleaned using ethanol. The fibers were fixed on one mount and hung over a second mount, as shown in Figure 24. The bare fiber sections were given three half twists, and a six-gram weight was attached to the fibers at the free end. Light from an 830-nm laser diode was launched through the fiber and the two outputs were monitored using amplified silicon detectors (Thor Labs PDA50). While under tension, the bare, twisted section of the fibers are heated, fused, and drawn. As the two fibers are fused together, light from the input fiber was coupled into the other fiber. This process was terminated when the desired coupling of light was achieved between the two output ports.

Fiber optic tapers were fabricated with Corning SMF 28 single mode fiber using the same process. This fiber has a core diameter of 9 μm and a clad diameter of 125 μm. The core refractive index is 1.4681 and the clad refractive index is 1.4450, as specified at 1550 nm by the manufacturer. The taper output intensity oscillated as the fiber was drawn out, and the process was stopped when the desired number of power oscillations had occurred.

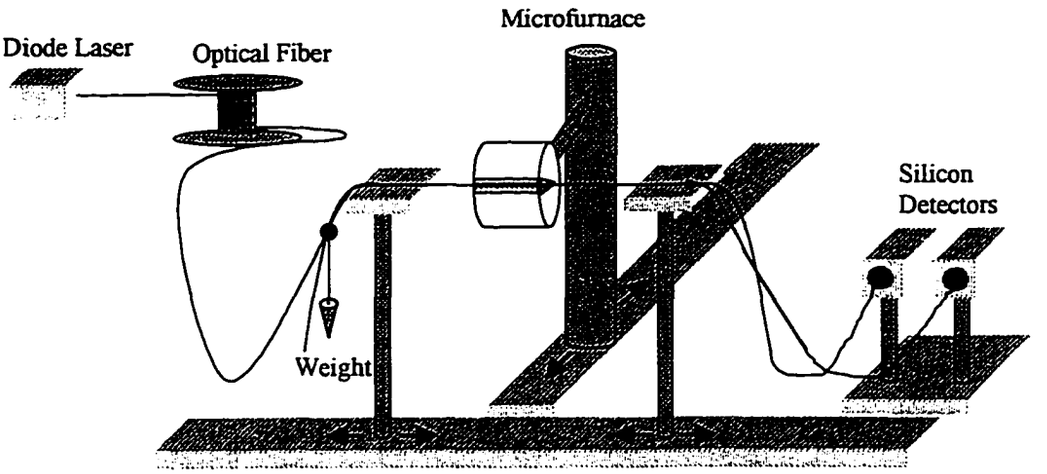

Figure 24: Experimental setup for fabricating fiber optic couplers. The same setup is used to fabricate fiber optic tapers, except only one detector/multimeter pair is required.

3.2 Preparation of Dyes and Solutions

The refractive index variation was achieved using solutions of dimethylsulfoxide (DMSO) in deionized water (DH_2O). DMSO has a refractive index of 1.4780, while that of DH_2O is 1.3333. The refractive index of a mixture of water and DMSO follows the Lorenz-Lorentz law. This law states that for a mixture of M materials which do not interact, the refractive index of the mixture can be calculated from[10]

$$\frac{\left(n^2-1\right)}{\left(n^2+2\right)}\cdot\frac{W}{\rho}=\sum_{j=1}^{M}\left(\frac{n_j^2-1}{n_j^2+2}\right)\cdot\frac{W_j}{\rho_j} \tag{54}$$

where W is the weight of the mixture, W_j is the weight of the j^{th} component in the mixture, n is the refractive index of the mixture, n_j is the refractive index of the j^{th} component of the mixture, ρ is the density of the mixture, and ρ_j is the density of the j^{th} component of the mixture. Mixing appropriate amounts of DMSO and DH_2O, eleven solutions of increasing refractive index were created. Accurate volumes were measured using an Eppendorf 1000 μL pipettor. 10 mL of each solution was made. The density of each solution was calculated, and refractive indices were measured using a Milton Roy Abbe-3L refractometer calibrated for operation at 589.3 nm (sodium D line). This refractometer has an accuracy of ±0.0001. Table 1 gives characteristics of each solution.

Table 1: Experimental details of the DMSO-DH_2O solutions.

Volume % DMSO	Volume % DH_2O	Total Volume (mL)	Density (g/mL)	Refractive index, n (λ = 589.3 nm)
0	100	10	.99261	1.333
10	90	10	1.00787	1.348
20	80	10	1.01478	1.363
30	70	10	1.03120	1.379
40	60	10	1.03113	1.395
50	50	10	1.04991	1.4114
60	40	10	1.04658	1.4267
70	30	10	1.06494	1.4414
80	20	10	1.06596	1.4548
90	10	10	1.07403	1.4664
100	0	10	1.08071	1.4771

Evanescent wave absorption was introduced by surrounding the coupler and taper with a solution containing a dye with well-known absorption properties. IR-140 and IR-780 laser dyes were used, which were obtained from Aldrich Chemical Company. IR-140 has a formula weight of 779.21 g/mol and a peak absorption wavelength of 823 nm. IR-780 has a formula weight of 667.12 g/mol and a peak absorption wavelength of 780 nm. Each was readily dissolved in DMSO, hence DMSO/DH_2O solutions containing either dye were easily made. It was experimentally verified that incorporation of these dyes into solution did not change the nominal refractive indices of the solution. This was done by checking the refractive index of the solution before and after adding the dye.

3.3 Transmission Measurement

Transmission measurements were performed to obtain spectral outputs of the fiber optic couplers and tapers. The refractive indices of the medium surrounding the fused and tapered regions were varied using DMSO/DH_2O solutions. Evanescent wave absorption on the spectral output of these couplers and tapers was investigated using solutions incorporating IR-140 or IR-780 laser dye and solutions without the laser dye. The percentage of DMSO in DH_2O was kept the same for all transmission measurements to assure that changes in the absorption characteristics, such as wavelength shifting, did not occur. Broadband emission from a quartz tungsten halogen white light source (Oriel 7340) was focused onto the input fiber using a 10x microscope objective. The coupler or taper was mounted inside a copper U-groove beam shown in Figure 25 so it was mechanically stable and could be immersed in the solution, which forms the external medium. The light output was collimated using a 20x microscope objective and focused onto the entrance slit of a Chromex 250IS imaging spectrograph using a 1-in. diameter f/4

lens. The dispersed light from the spectrograph was imaged onto an SBIG ST6 silicon CCD array. The computer-interfaced data gave the output intensity versus pixel number. The spectra were collected in the dark to minimize background noise. Pixel numbers were converted to wavelength scale using the spectral output of an Oriel 6034 Hg/Ne calibration lamp. The experimental arrangement used for these transmission measurements is shown in Figure 26.

3.4 Infrared Absorption Spectroscopy of Laser Dye Solutions

The absorption bands for IR-140 and IR-780 laser dyes were determined using infrared spectroscopy. A Varian Cary 3Bio UV-Vis spectrophotometer was used to collect the absorbance spectra from 500 – 900 nm. Because the spectrophotometer was a dual-beam instrument, DMSO/DH_2O solution without dye was used in the reference beam. The absorbance spectrum of the dye was obtained after the Cary 3 software performed the required intensity ratio, as given by

$$A = \log \frac{I_o}{I}. \tag{55}$$

where I_o is the intensity of light through the reference and I is the intensity of light through the sample. A Nicolet Magna-IR System 750 FTIR was used to measure the absorbance spectra from 900 – 1100 nm. The FTIR is a single-beam instrument, hence, OMNIC 3.1A software supplied by Nicolet was used to calculate the absorbance spectrum.

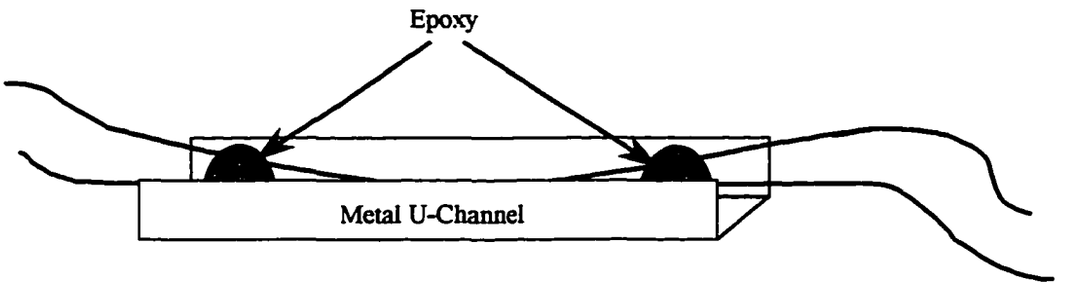

Figure 25: U-channel groove used to mount the fiber optic couplers and tapers.

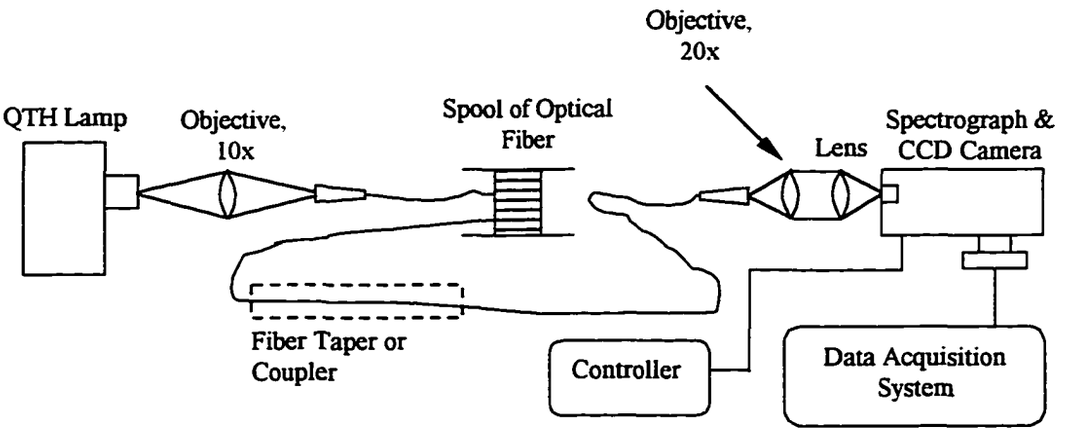

Figure 26: Experimental setup for optical dispersion measurements using a fiber optic taper or coupler.

CHAPTER IV

RESULTS AND DISCUSSION

A series of spectroscopic measurements was conducted on fiber optic coupler and taper devices to examine the effect of normal and anomalous dispersion. The spectral outputs were acquired by a CCD camera using a white light source, which was focused onto the input fiber of the device. The refractive index of the medium surrounding these devices was varied by using solutions of DMSO in DH_2O. Evanescent wave absorption was introduced by adding either IR-140 or IR-780 dye into the DMSO/DH_2O solutions. By adding different amounts of DMSO in DH_2O, the refractive index could be varied from 1.3333 to 1.4780. Figure 27 shows a plot of refractive index versus percent of DMSO in solution for the mixtures used in the research. A 'best-fit' second-order polynomial regression was performed and plotted in Figure 27 as a solid line. A plot of the density of solution is given in Figure 28. Using the experimental values for density and refractive index, the refractive index predicted by the Lorenz-Lorentz law (Equation 54) for each mixtures is plotted in Figure 29a, with a best fit line plotted for reference. Figure 29b shows a comparison of the best fit values of refractive index obtained from experiment and from Lorenz-Lorentz law. Although the experimental data follow a quadratic dependence, the Lorenz-Lorentz law predicts very well the refractive index of each mixture based only on the refractive indices, densities, and weight percentages of the components. Hence, we expect the refractive index of the DMSO/DH_2O mixture to increase with increasing weight percent of DMSO.

Evanescent wave absorption was introduced by dissolving an absorbing dye in the DMSO/DH_2O solutions. IR-140 and IR-780 are both laser dyes that have strong

absorption bands in the near infrared when dissolved in a solution of DMSO/DH_2O. A typical absorption spectrum for IR-140 is given in Figure 30. Here, 0.15 mmol/L IR-140 is mixed using a 72% DMSO-28% DH_2O solution, and a strong absorption peak near 815 nm is evident. This absorption peak has a FWHM of approximately 95 nm. Similarly, absorption spectrum for IR-780 is given in Figure 31, where 0.15 mmol/L IR-780 is mixed using a 72% DMSO-28% DH_2O solution. A strong absorption peak near 790 nm with a FWHM of approximately 65 nm is evident. These absorption peaks will be used to induce evanescent wave absorption, and hence anomalous dispersion, on the fiber optic couplers and tapers.

Fiber optic couplers were fabricated using the fuse, pull, and taper method. The couplers became more sensitive to external refractive index as the number of power oscillations increased. However, only five or fewer power oscillations could be achieved since the tapered region became very fragile. A coupler was drawn out until 4.25 power oscillations occurred. The spectral output of such a coupler is shown in Figure 32. The sinusoidal variation is distorted when air is the surrounding medium. This is due to weak mode beating in the coupled region since the refractive index difference between air the fiber cladding is large. However, Figure 33 shows the same coupler when immersed in water. With a smaller refractive index difference between water and the fiber cladding, strong sinusoidal variation with wavelength is seen. The output from Port 3 and 4 are also complementary, and these results are expected based on coupler theory presented in Section II.2. The coupler was also immersed in different mixtures of DMSO/DH_2O to vary the refractive index of the medium surrounding the coupler region. For a three-power-oscillation coupler, the resulting spectral output for Port 3 is shown in Figure 34.

As the refractive index of the external medium becomes closer to that of the fiber cladding, the period of the spectral oscillations becomes larger. This is because as the difference ($n_2^2 - n_3^2$) decreases, the V-parameter also decreases. This in turn causes the coupling coefficient to decrease and the period of output power oscillations given by Equations 29 and 30 to increase. Figure 34 also shows an important effect on the spectral shift of the maxima and minima with refractive index. As n_3 increases, the wavelength shifts of both maxima and minima increase. This experimental result was shown theoretically in Figure 10. It is important to note that for normal dispersion, n_3 increases with decreasing wavelength. A significant result then follows. *For normal dispersion, as wavelength decreases, the wavelength shifts of maxima and minima increase.* This important result will be used to discriminate between normal dispersion and anomalous dispersion in the coupler and taper results to follow.

To examine the effect of evanescent wave absorption on the coupler output, appropriate amounts of IR-140 or IR-780 were mixed in to the DMSO/DH_2O solution. In particular, a 72% - 28% DMSO/DH_2O mixture was used since its refractive index (1.4449) is lower than that of the fiber cladding. The dye was dissolved in the solution to produce 0.15 mmol/L solution. The spectral output P_3 of a $3\frac{1}{8}$-power-oscillation coupler is shown in Figure 35a. The reference and dye solutions were made to have the same nominal refractive index. Hence, the spectral outputs of the coupler immersed in the reference solution and in the dye solution should be identical, except for any changes due to evanescent wave absorption and Kramers-Kronig effect. By comparing 1 and 2 in Figure 35a, evanescent wave absorption is readily evident as a decrease in the spectral intensity in the wavelength region near the 815 nm absorption band. The calculated

absorbance from Figure 35a is shown in Figure 35b. A closer look at Figure 35a also reveals a spectral shift between the maxima and minima of the two outputs. A plot of the wavelength shift between the two outputs is shown in Figure 36. If there is no dispersion, then the maxima and the minima of the two outputs should coincide. However, recall the important result that for normal dispersion, as wavelength decreases, refractive index increases, and the wavelength shift of the maxima and minima increases. In Region 1 of Figure 36, the wavelength shift is seen to increase with decreasing wavelength from 970 to 875 nm, corresponding to normal dispersion. In Region 2, which is within the absorption band, however, the wavelength shift steadily decreases for decreasing wavelength from 875 to 715 nm. This corresponds to a refractive index *that decreases with decreasing wavelength*, which is *anomalous dispersion*. Thus, anomalous dispersion induced by the evanescent wave absorption is clearly demonstrated. Fabricating a more sensitive coupler can enhance this effect, however, this requires drawing the coupler out more such that the waist diameter is further reduced. This is difficult because such couplers are too fragile to handle. This is a major drawback in using couplers to study anomalous dispersion induced by absorption.

Fiber optic tapers were fabricated using the pull and taper method. As the taper was drawn out, the output power was monitored using a semiconductor laser and detector, and the output power was seen to oscillate during the process. A typical pull signature showing this power oscillation is shown in Figure 37a, with a magnified view shown in Figure 37b. The fabrication was stopped when the required number of power oscillations had occurred. As in the case of a coupler, the taper was immersed in mixtures of DMSO and DH_2O to examine the spectral output as a function of external

refractive index. In Figure 38, the period of the oscillations becomes larger as the refractive index of the external medium (i.e. the DMSO/DH_2O solution) increases. This is similar to what was seen for the case of couplers immersed in solutions of varying refractive indices. This was the case for all tapers fabricated and tested in this manner. The taper shown in Figure 38 was fabricated with approximately 105 power oscillations.

The effect of evanescent wave absorption on the spectral output of tapers was studied using appropriate dye mixed in the DMSO/DH_2O solutions. The reference and dye solutions used in the couplers experiments were also used for the taper experiments. The taper used in Figure 38 was immersed in the reference solution and in the dye solution, and the spectral outputs were recorded, as shown in Figure 39. The spectral outputs are nearly identical in spectral phase since the reference and dye solutions have the same nominal refractive index. However, two effects can be seen. Evanescent wave absorption can be seen near the absorbing wavelength of IR-140 (~ 815 nm) as a reduction in the spectral intensity of the spectral oscillations. A closer look at Figure 39 also reveals a spectral shift between the two outputs near 815 nm. When a wavelength shift between the two outputs is measured, the plot shown in Figure 40 is obtained. In Region 1, the refractive index increases as the wavelength decreases as expected from normal dispersion, and hence the wavelength shift increases. In Region 2, the refractive index decreases with decreasing wavelength due to anomalous dispersion, leading to a decreasing wavelength shift. This is a clear indication of anomalous dispersion. In Region 3, normal dispersion occurs, and the wavelength shift increases again as the wavelength decreases. The shift in the spectral output occurs only for a change in refractive index, and the wavelength shift has a shape that is similar to that of anomalous

dispersion in refractive index near an absorption band. A spectral calibration of the wavelength shifts was obtained by immersing the taper in solutions with different refractive indices and calculating the shifts for each wavelength. The spectral calibration curves are shown in Figure 41. Using these calibration curves, dispersion seen in Figure 39 is plotted in Figure 42. The refractive index change due to normal dispersion is much smaller than the refractive index change due to anomalous dispersion shown between 755 and 900 nm. Similar experiments were done on a taper immersed in a DMSO/DH_2O solution containing IR-780 dye. The spectral outputs for a 110-power-oscillation taper immersed in a reference containing 72% - 28% DMSO/DH_2O and in a solution containing the same reference plus 0.15 mmol/L IR-780 are shown in Figure 43. Evanescent wave absorption is seen near 795 nm as a reduction in the spectral peak intensities of the oscillations. More important is the variation of the wavelength shift between the two spectral outputs, as shown in Figure 44. Just as in Figure 38 for a taper immersed in a solution containing IR-140, Region 1 shows a wavelength shift increase due to normal dispersion, Region 2 shows a wavelength decrease due to anomalous dispersion near 795 nm, and Region 3 shows a wavelength shift increase due to normal dispersion.

It is clearly demonstrated that Kramers-Kronig effect occurs due to the presence of evanescent wave absorption. Fiber optic couplers and tapers have been shown to be useful in examining this effect in the presence of absorption due to their high sensitivity to refractive index of the surrounding medium.

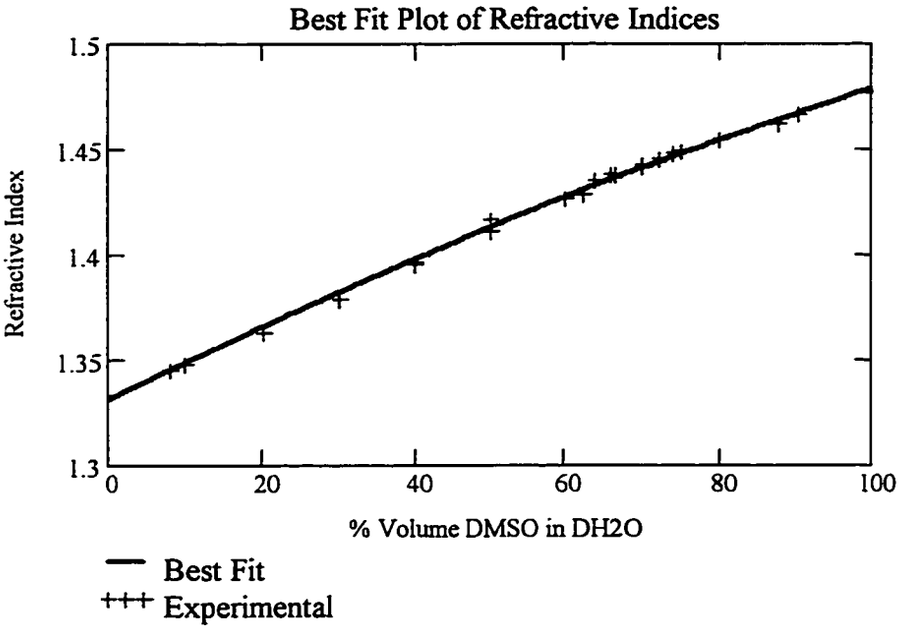

Figure 27: Measured refractive indices for solutions of DMSO in DH_2O (λ = 589.3 nm). The solid line represents the 'best fit' second order polynomial regression to the measured values.

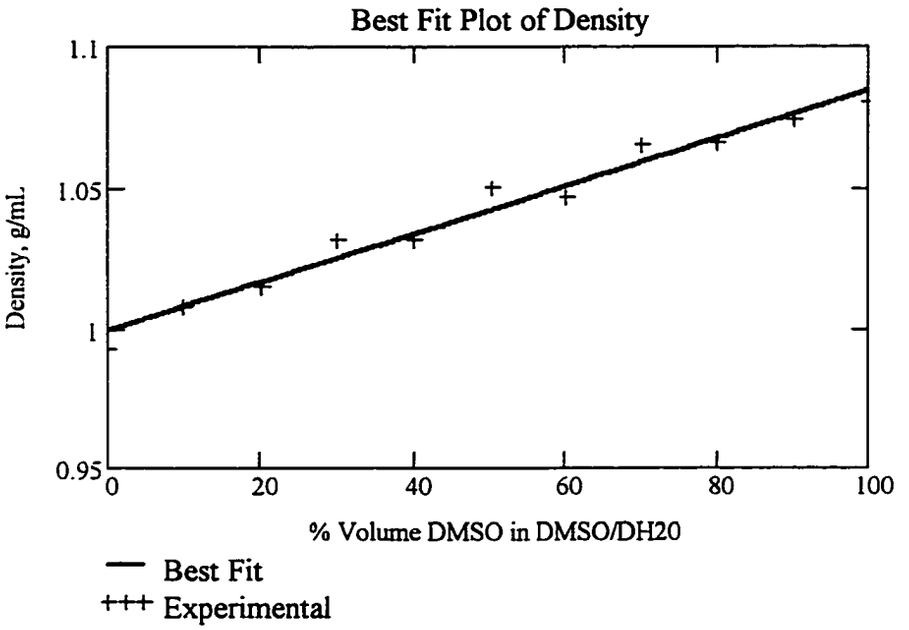

Figure 28: Calculated densities for solutions of DMSO in DH_2O. The solid line represents the 'best fit' linear regression to the calculated values.

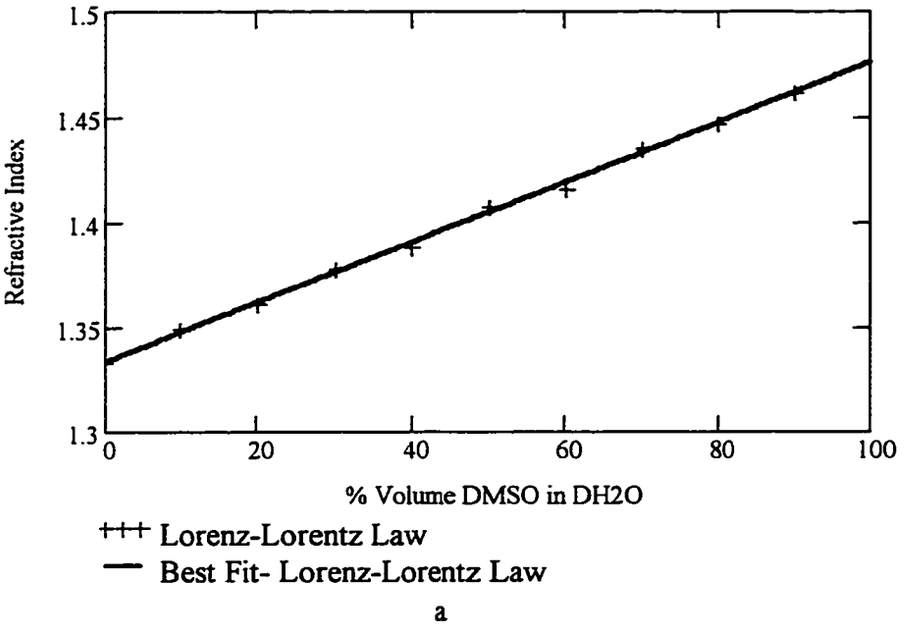

a

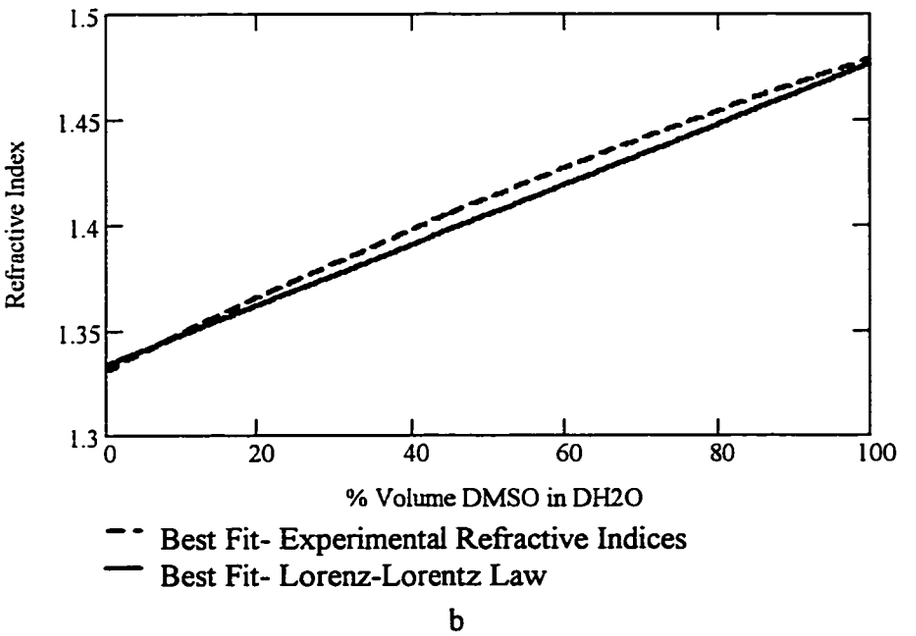

b

Figure 29: a) Calculated and best fit values of refractive index using Lorenz-Lorentz law. The density values shown in Figure 28 are used. b) Comparison of the best fit values of refractive index obtained from experiment and from Lorenz-Lorentz law.

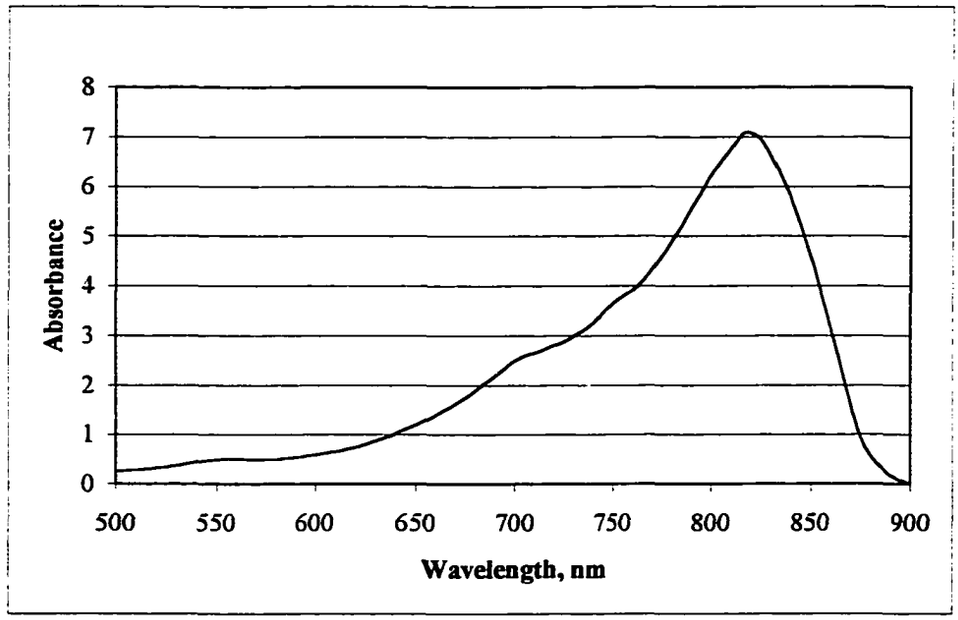

Figure 30: Absorbance spectrum of 0.15 mmol/L IR-140 in 72% - 28% DMSO/DH_2O solution.

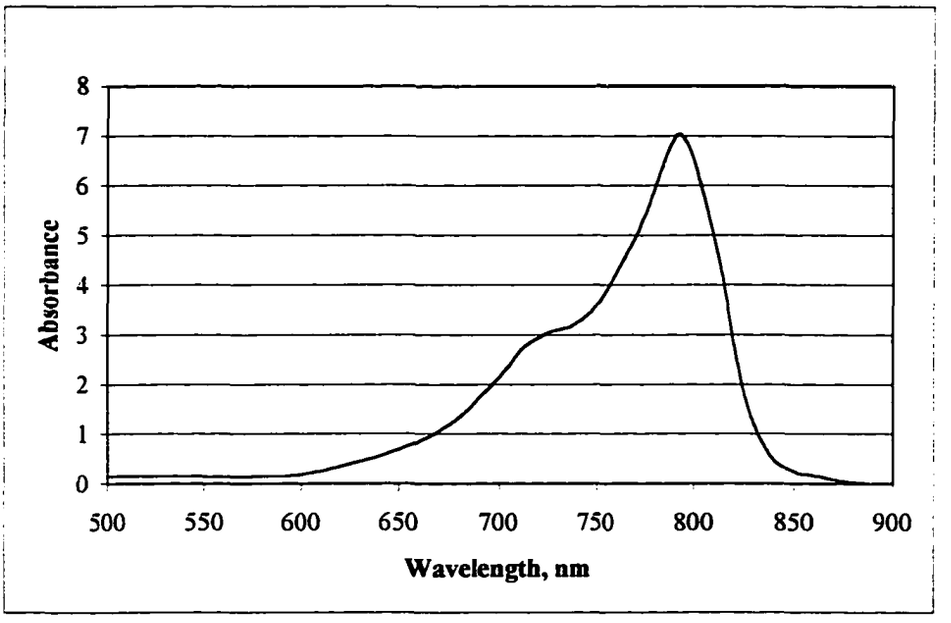

Figure 31: Absorbance spectrum of 0.15 mmol/L IR-780 in 72% - 28% DMSO/DH_2O solution.

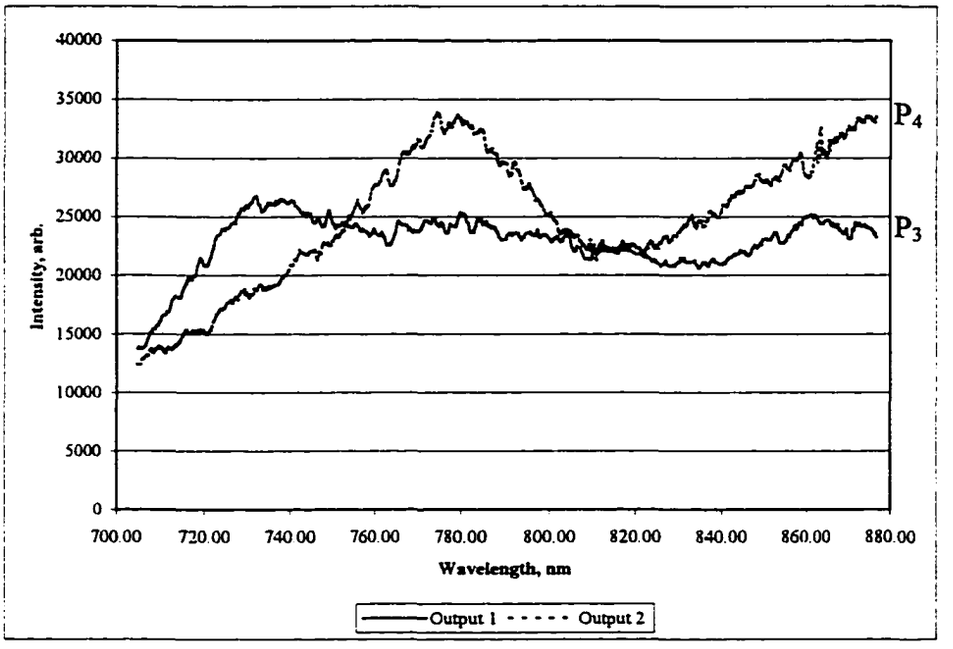

Figure 32: Spectral outputs from Port P_3 and P_4 for a 4.25-power-oscillation coupler. The external medium is air.

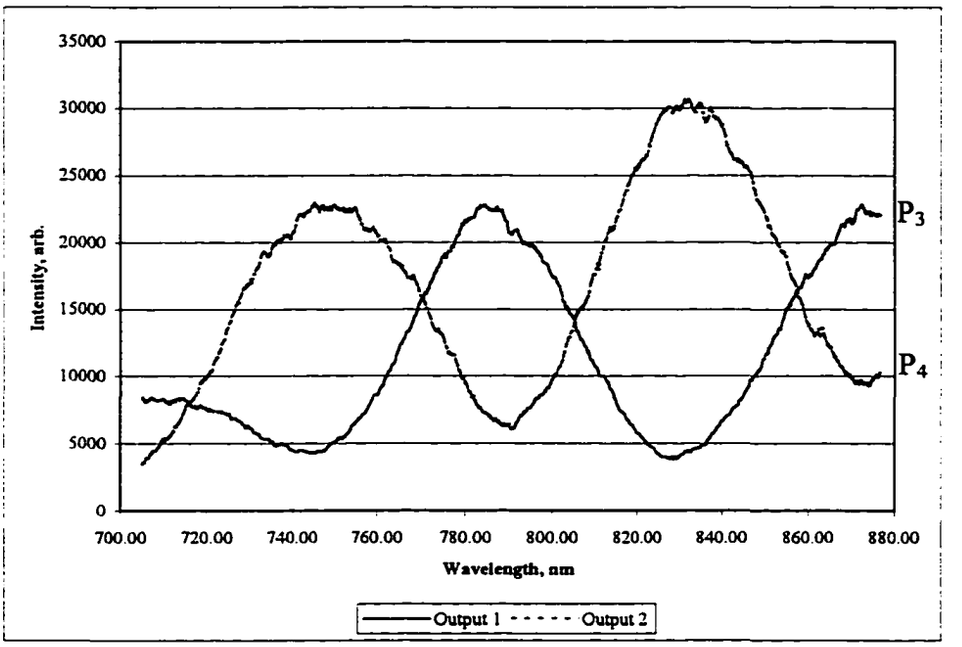

Figure 33: Spectral outputs from Port P_3 and P_4 for a 4.25-power-oscillation coupler. The external medium is water.

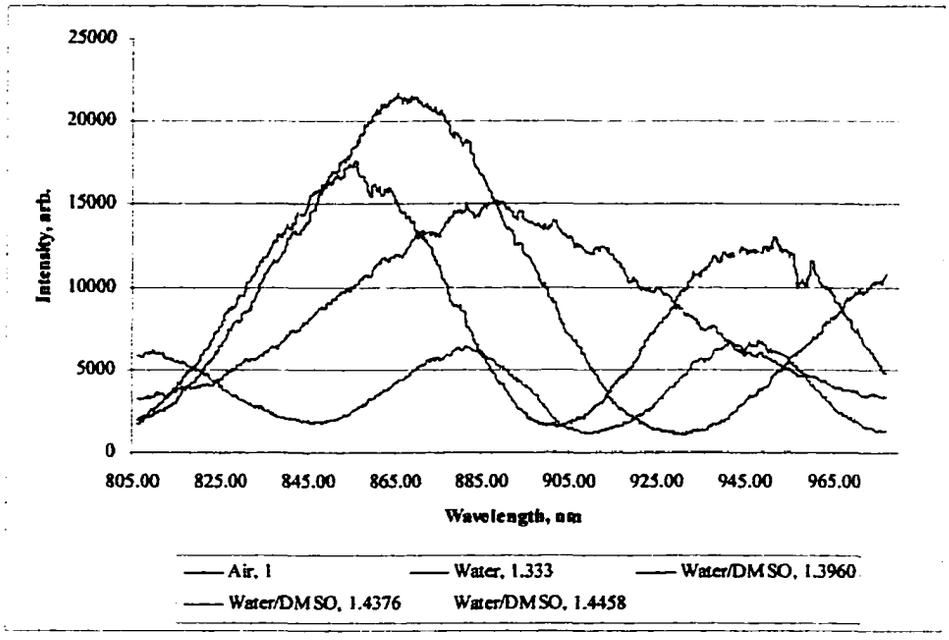

Figure 34: Spectral output from Port P_3 of a 3-power-oscillation coupler for different refractive indices for the external medium.

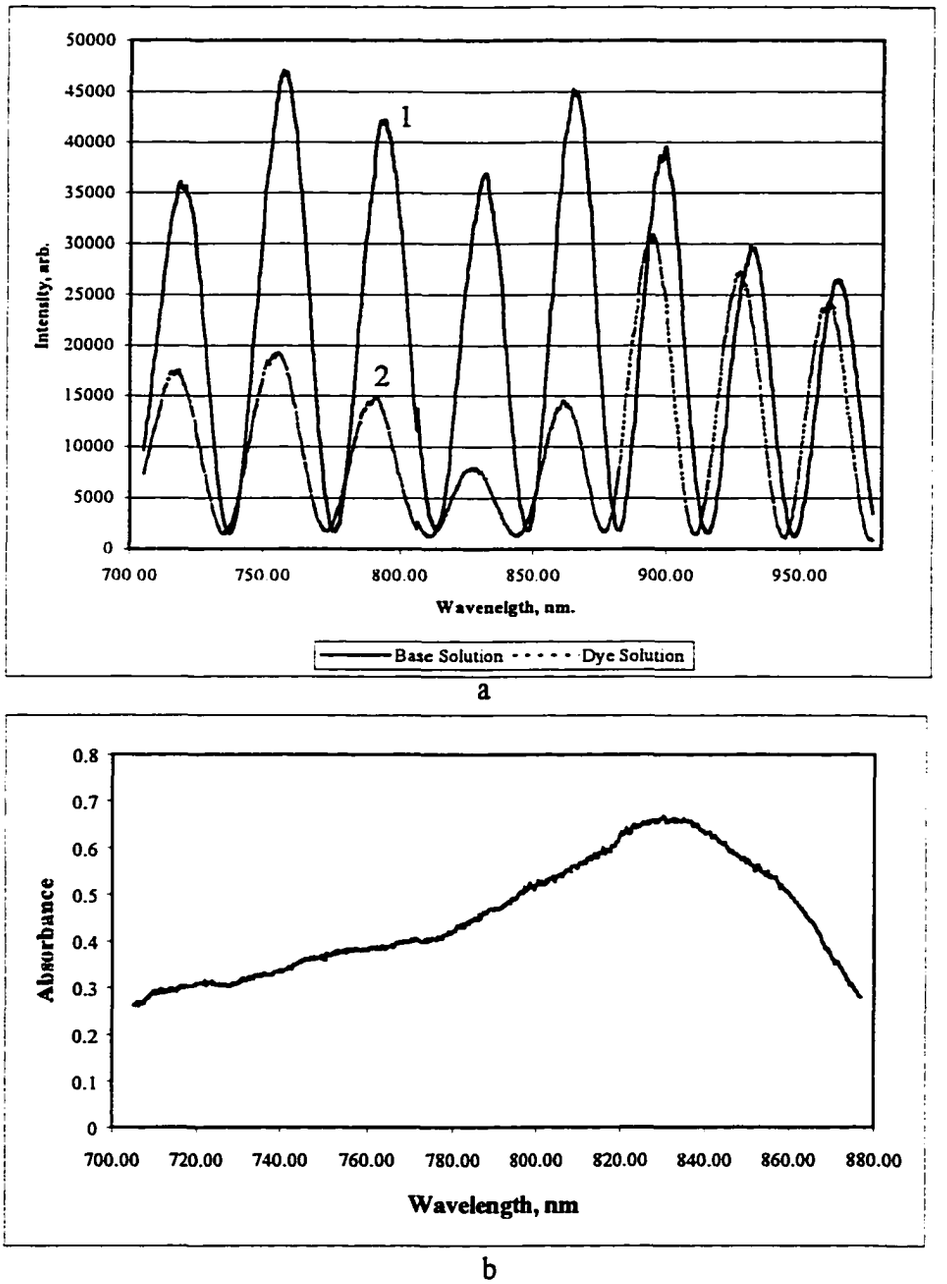

Figure 35: a) The spectral output P_3 of a 3.125-power-oscillation coupler immersed 1) in a reference solution and 2) in a dye solution. Reference solution: 72-28% DMSO/DH_2O, Dye Solution: 0.15 mmol/L IR-140 in reference solution. For both, n=1.4449. b) Absorbance calculated from coupler outputs using Equation 38.

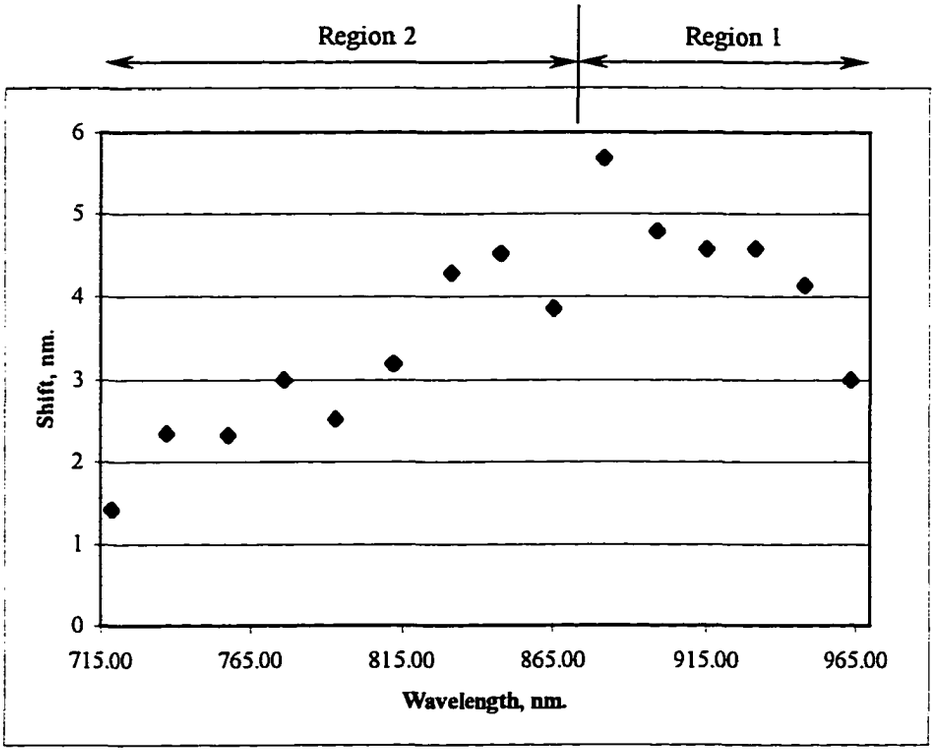

Figure 36: The calculated wavelength shift for the output power P_3 shown in Figure 35.

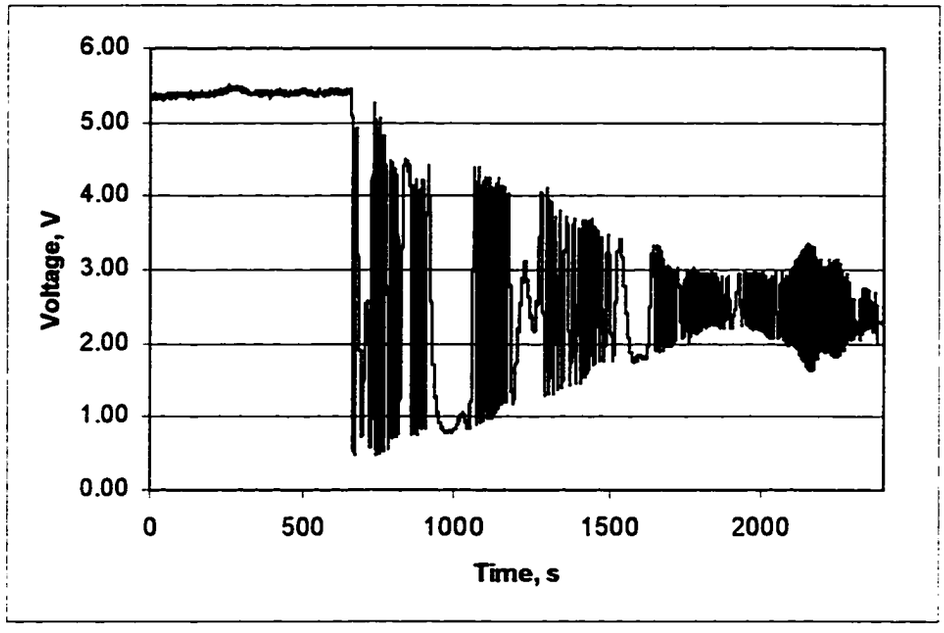

a

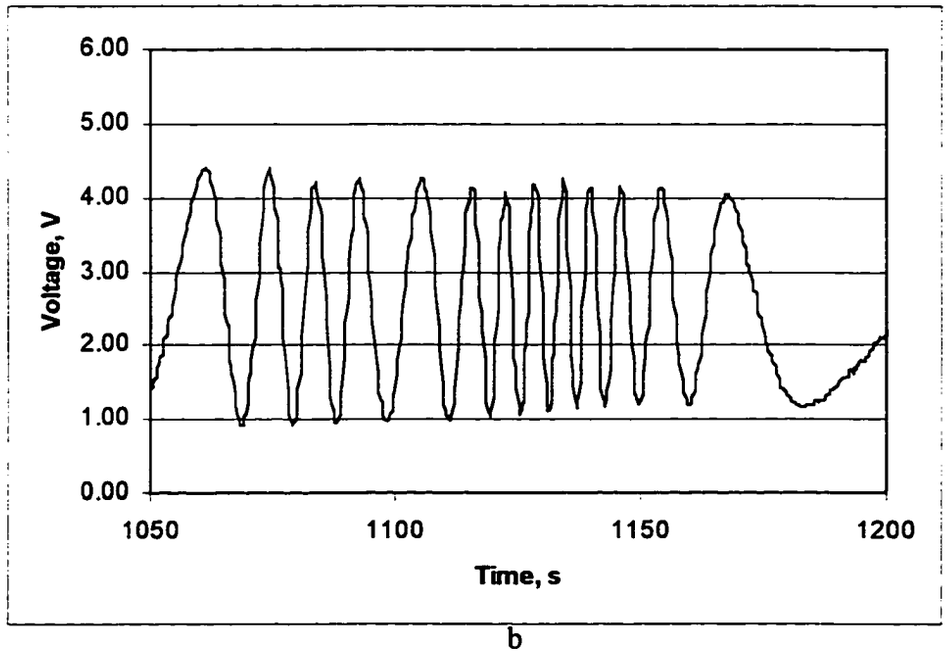

b

Figure 37: a) Typical pull signature during fabrication of a fiber optic taper. b) Expanded view of pull signature showing the power oscillations as the taper is drawn out in time.

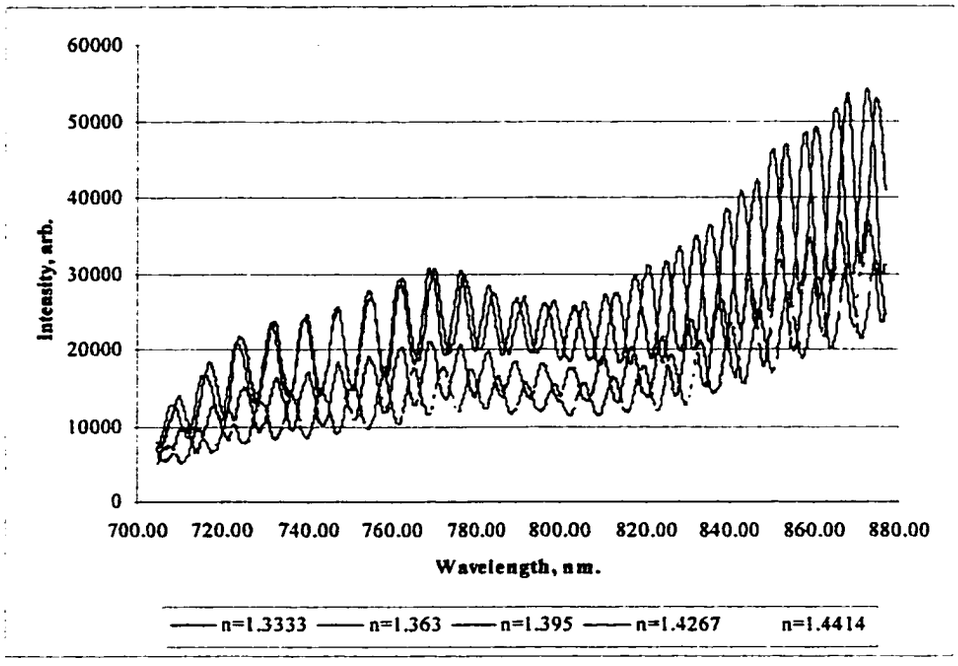

Figure 38: Spectral output versus external refractive index for a 105-power-oscillation taper.

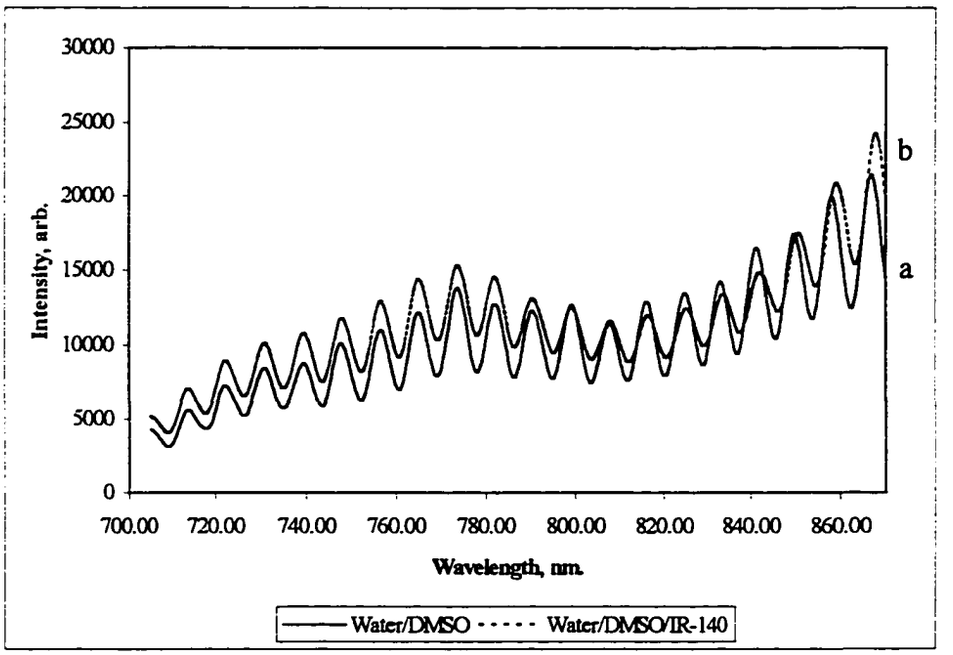

Figure 39: Spectral output of a 105-power-oscillation taper immersed a) in a reference solution of 72% - 28% DMSO/DH_2O and b) in the reference solution dissolved with 0.15 mmol/L IR-140 dye.

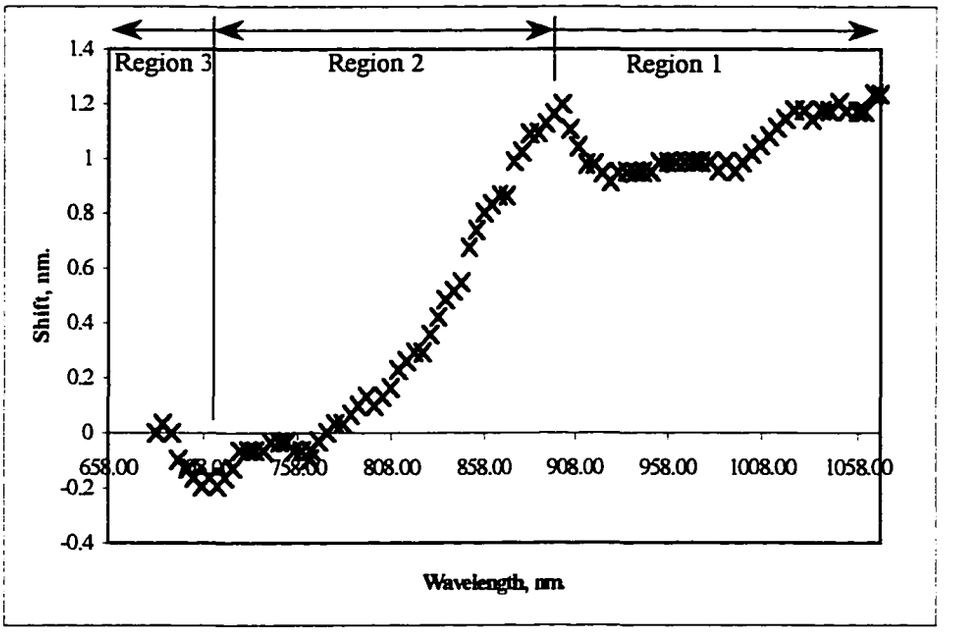

Figure 40: The calculated wavelength shift between the two outputs shown in Figure 39.

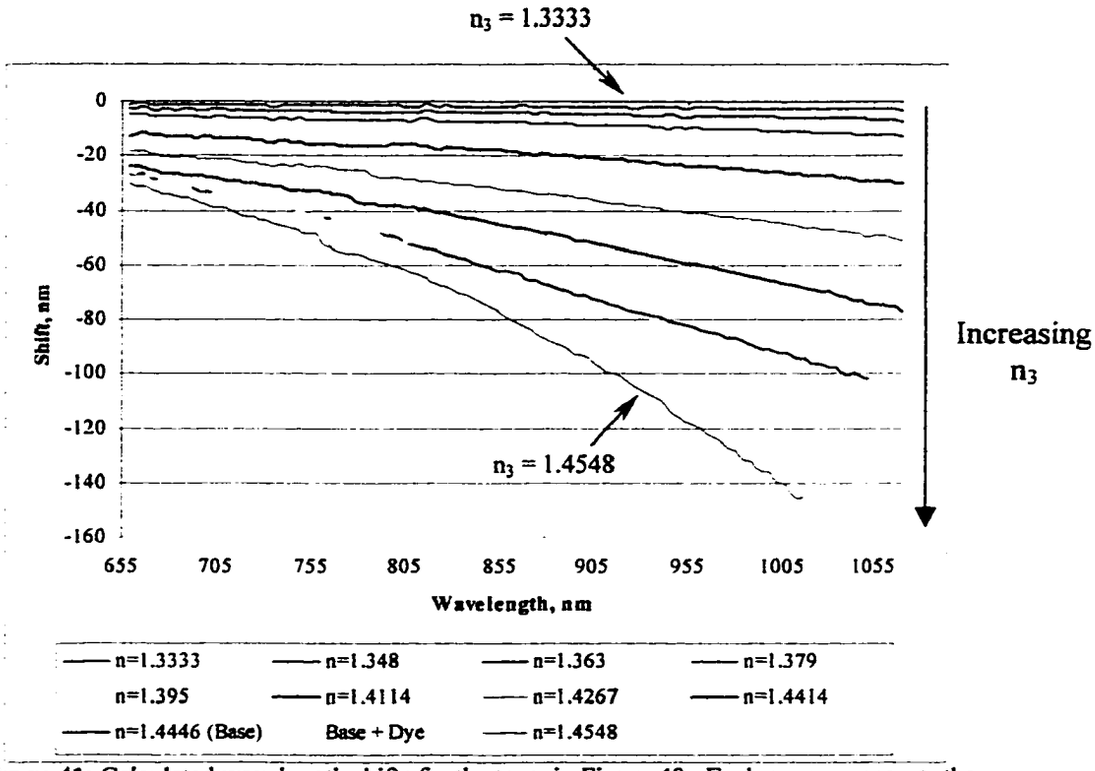

Figure 41: Calculated wavelength shifts for the taper in Figure 40. Each curve represents the wavelength shift due to immersing the taper in solutions with different refractive indices. The reference and dye solutions have a nominal refractive index of 1.4443.

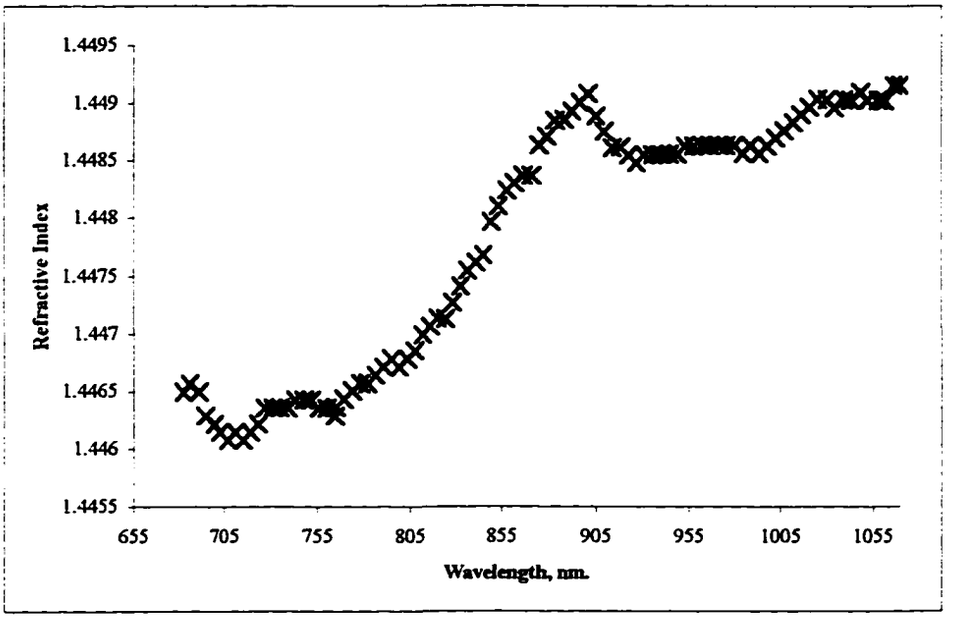

Figure 42: Dispersion plot of the wavelength shift shown in Figure 40 using the calibration curves obtained in Figure 41.

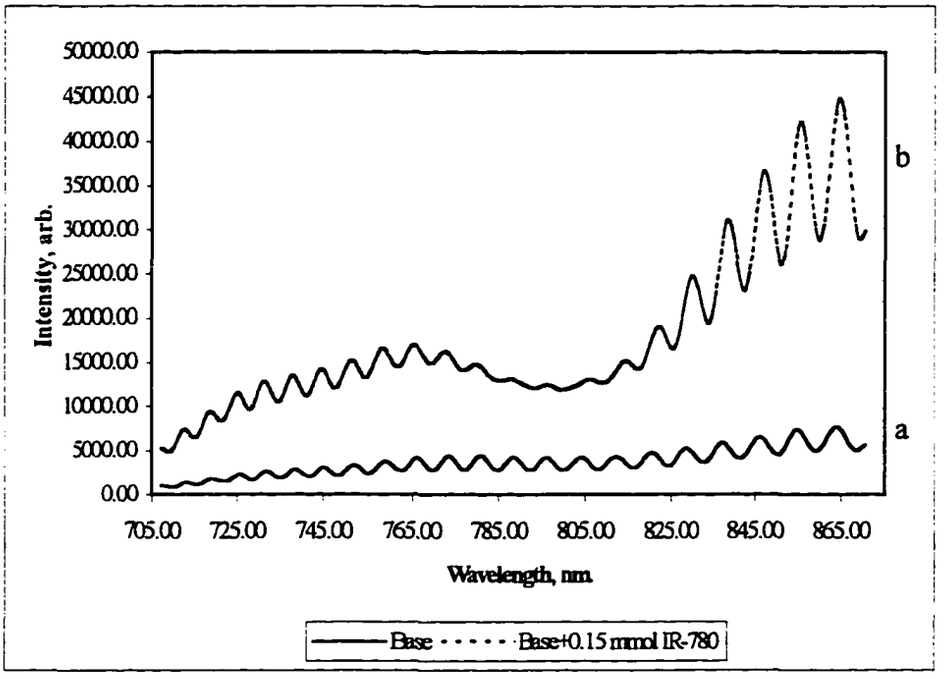

Figure 43: Spectral output of a 105-power-oscillation taper immersed a) in a reference solution of 72% - 28% DMSO/DH_2O and b) in the reference solution dissolved with 0.15 mmol/L IR-780 dye.

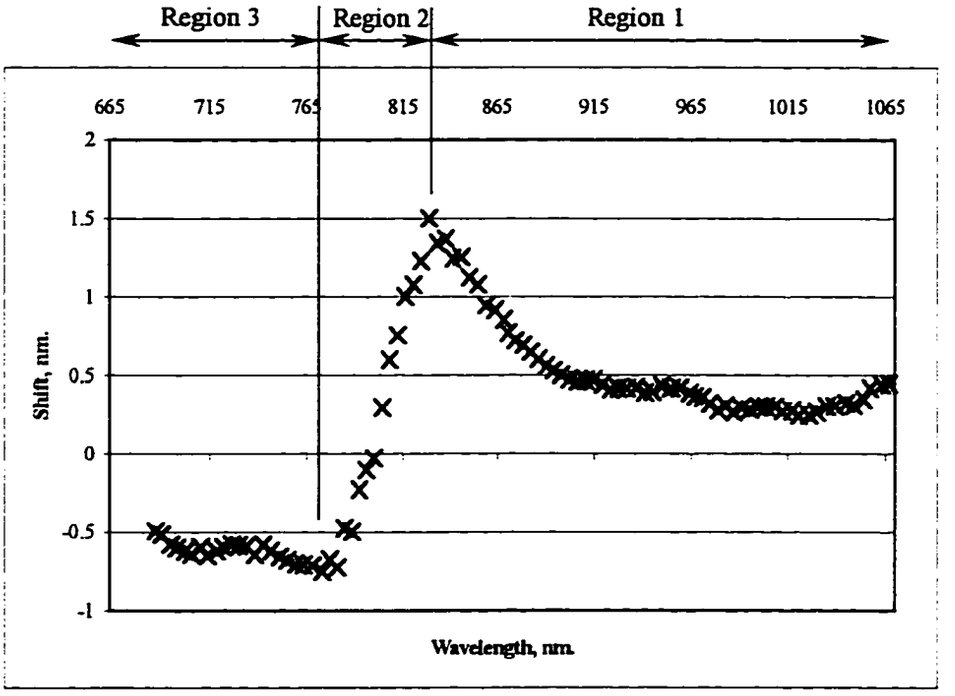

Figure 44: The calculated wavelength shift between the two outputs shown in Figure 43.

CHAPTER V

SUMMARY AND APPLICATION

The refractive index of a medium is an important parameter in understanding the operation of FOS. Because of optical dispersion, the sensing and light-guiding properties of FOS will change with wavelength. FOC's and FOT's are especially affected by optical dispersion, as discussed in Chapter II. This opens up the possibility of using couplers and tapers to detect anomalous dispersion, or Kramers-Kronig effect, associated with the presence of evanescent wave absorption.

5.1 Kramers-Kronig Effect on FOC's

In Section II.2, it was shown that FOC's have an oscillatory spectral output. These oscillations are dependent on the strength of coupling from the fundamental mode of one fiber to the other. Assuming a rectangular fused region, the coupling coefficient is shown to be dependent highly on the refractive indices of both the fiber clad and the medium surrounding the fused region of the coupler. The effect of the refractive index of the external medium on the spectral output of couplers was studied. Light propagating through the coupler will also suffer two types of absorption losses: one due to the fiber core/clad and the other due to evanescent wave absorption losses from absorbing species in the surrounding medium. Theoretical studies have shown that the coupler is a very useful device to discriminate between evanescent wave absorption and dispersion [39]. Both evanescent wave absorption and dispersion are clearly demonstrated experimentally using a 2 x 2 biconically fused fiber coupler. In particular, this is the first study of anomalous dispersion reported on couplers. It appears that for sensitive detection of dispersion, the coupling coefficient should be increased further. Current fabrication

method necessitates a thinner diameter for the fused region, making the coupler mechanically unstable.

5.2 Kramers-Kronig Effect on FOT's

The theoretical expressions showing the oscillatory power output of a fiber optic taper were given in Section II.3. The taper output is more sensitive to external refractive index change of the external medium. Hence, a taper is a useful device for detecting anomalous dispersion. Experiments conducted on a highly sensitive taper have clearly demonstrated Kramers-Kronig anomalous dispersion for the first time [40]. A fiber taper appears to be a better device than a 2 x 2 coupler for optical absorption and dispersion studies.

5.3 Applications

Optical absorption is a characteristic property of a medium. Kramers-Kronig effect on tapers can effectively be used for chemical sensing. The wavelength region where anomalous dispersion occurs can be estimated by differentiating n in Equation 20 [10]. The refractive index has a maximum and a minimum at $\lambda_{1,2} = 2\pi c\left(\frac{4\pi^2 c^2}{\lambda_o^2} - \frac{\omega_p^2}{3} \mp \frac{\gamma}{2}\right)^{-1}$, respectively. The change in refractive index in terms of λ_o is obtained as [39]

$$\Delta n = n(\lambda_1) - n(\lambda_2) \tag{56}$$

where Equation 23 is used for the refractive index for dense media.

The important result in Equation 56 is that the change in refractive index is proportional to number of atoms per unit volume of the medium and to the resonance absorption wavelength, just as in the case of gaseous media. For a dense medium with

multiple absorption bands, a longer wavelength dispersion measurement enhances the sensitivity.

In the case of a coupler, Figure 23 shows that the change in output power ΔP induced by Kramers-Kronig effect is proportional to Δn if the coupler is operated in the linear output range. A coupler fabricated under tight coupling condition is capable of detecting changes in n_3 smaller than 10^{-4} [14, 38]. Using an absorption line at 1550 nm for a medium, Equation 56 gives approximately $N = 3 \times 10^{20}$ atoms·m^{-3}. This concentration is about ten parts per million. Hence, it is conceivable that a biconically tapered fiber coupler can serve as a chemical sensor using Kramers-Kronig effect.

A similar argument holds true for tapers too. In Figure 41, the spectral output of a taper immersed in a 0.15 mmol/L IR-140 solution is shown. This corresponds to a concentration of approximately $9.0 \cdot 10^{22}$ m^{-3}. The change in refractive index due to anomalous dispersion is $\Delta n \approx 2.75 \cdot 10^{-3}$. Using Equation 56, the concentration calculated due to anomalous dispersion is $1.56 \cdot 10^{24}$ m^{-3}. This is a factor of 17 larger. The main cause for error is from accurately measuring the wavelength shift in the spectral outputs shown in Figure 38. In the region of anomalous dispersion, evanescent wave absorption reduces the signal-to-noise ratio. It could be improved by using modulation detection techniques.

Another source of error comes from the classical theory of optical dispersion, which assumes a single absorption line with a Lorentzian lineshape. Because of the complexity of the chemical structure of the dye used, the absorption line should more accurately be modeled as a collection of narrow Lorentzian lines with resonance wavelengths slightly shifted from that of the central absorption wavelength. The total

lineshape would be due to the summation of the individual narrow Lorentzian lineshapes. By the Kramers-Kronig relations, the total refractive index profile would be a summation of the refractive index profiles due to each of the individual Lorentzian lineshapes. This "inhomogeneous broadening" of the absorption and refractive index profiles occurs because atoms at different crystal sites see slightly different local surroundings and crystal structure, leading to slight variations in the transition wavelengths. Better agreement with experimental data could be achieved using this modified lineshape.

A third source of error comes from the calibration curve used in Figure 41 to obtain the refractive indices from the wavelength shifts. Figure 41 shows that for a particular wavelength, as the refractive index increases, the magnitude of the wavelength shift increases. For normal dispersion, an increasing refractive index occurs for decreasing wavelengths. Thus, the magnitude of the wavelength shift should increase for decreasing wavelengths for normal dispersion, and this is correctly shown in Figure 40. However, the spectral periods of the coupler and taper outputs are also dependent on the refractive index. Thus, Figure 40 will show a combined effect due to dispersion and to the dependence of the spectral period to refractive index. An error in the refractive indices obtained using this calibration curve will be present since the change in spectral period due to refractive index was not accounted for.

It is important to note that the chemical sensing technique using Kramers-Kronig effect on couplers and tapers does not require an absorbing coating on the sensor; therefore, diffusion and related reversibility problems may not limit it. Hence, it is suitable for in-situ real-time monitoring applications. Further, since the resonance

absorption is unique to each absorbing species, the Kramers-Kronig sensor will be highly selective. The dispersion effect can easily be distinguished from usual fiber losses.

Conventional absorption spectroscopy makes use of the imaginary part of the dielectric constant given in Equation 20, whereas, in this study, the real part of the dielectric constant is employed. To increase the sensitivity of the former method, the optical path length must be increased, usually with a multipass or White cell arrangement, making the instrument large and bulky. The outputs of coupler and tapers repeat themselves for every (CL) = 2π, therefore, these devices can be compact and small.

5.4 Future Work

Much work still needs to be done before highly sensitive measurements of anomalous dispersion can be made. The coupler and taper spectral response must be optimized for high sensitivity to the refractive index of the surrounding medium. Thus, a more detailed study of the parameters affecting the sensitivity of the devices is required. In Section II.2, the coupling coefficient C was obtained by assuming that the fused region of a coupler was modeled as a rectangle. This cross-section should more properly be modeled as an ellipse or two touching circles. Since the choice of cross-sectional geometry will affect the coupler response and sensitivity to refractive index, each cross-section must be evaluated to determine which most accurately models the fused region.

Another issue that requires further investigation is the effect of polarization on the sensitivity of couplers and tapers. In Section II.2, the possibility of incorporating polarization effects in the theoretical modeling was discussed. However, these effects were not included to make the analysis easier. Theoretical and experimental work should

be done to examine the spectral response and the sensitivity of couplers and tapers that exhibit polarization properties.

Another area of investigation is the fabrication technique for couplers and tapers. The devices used in this research were made manually. Thus, recreating the same conditions to fabricate similar couplers or tapers is extremely difficult. A computer-controlled heating and drawing assembly could be used to accurately control the heater temperature, fiber elongation, and heater motion to obtain repeatable fabrication of couplers and tapers. Also, once made, these devices must be properly packaged to provide stability and protection.

Finally, in Section II.3, the spectral output of tapers was shown to be oscillatory with wavelength. This is due to the mode beating that occurs between the two lowest order modes, HE_{11} and HE_{12}. However, it is possible for higher order modes, such as HE_{13}, to propagate and interact with these lower order modes. It is not known how multiple modes will affect the response and sensitivity of tapers to refractive index.

REFERENCES

[1] K. Yamamoto, A. Masui, H. Ishida, Appl. Opt., **33**, 6285, 1994.

[2] K. Yamamoto, H. Ishida, Spectrochimica Acta., **50A**, 2079, 1994.

[3] D. A. Nolan, P. E. Blaszyk, E. Udd, Fiber Optic Sensors: An Introduction for Engineers and Scientists, ed. E. Udd, John Wiley & Sons, Inc., New York, 1991.

[4] L. C. Bobb, H. D. Krumboltz, J. P. Davis, Proc. SPIE, **990**, 164, 1988.

[5] A. Harmer, A. Scheggi, in Optical Fiber Sensors: Systems and Applications, ed. B. Culshaw, J. Dakin, Artech House, Norwood, 1989.

[6] N. J. Harrick, Internal Reflection Spectroscopy, John Wiley and Sons, New York, 1979.

[7] "Test method for Thickness of Epitaxial Layers of Silicon on Substrates of the Same Type by Infrared Reflectance", Annual Book of ASTM Standards, F95-89, American Society for Testing and Materials, Philadelphia, 1989.

[8] R. W. Christy, Am. J. Phys., **40**, 1403, 1972.

[9] F. L. Pedrotti, L. S. Pedrotti, Introduction to Optics, Prentice Hall, New Jersey, 1993.

[10] R. Guenther, Modern Optics, John Wiley & Sons, New York, 1990.

[11] C. Kittel, Introduction to Solid State Physics, John Wiley & Sons, New York, 1966.

[12] F. P. Payne, C. D. Hussey, M. S. Yataki, Elect. Lett., **21**, 461, 1985.

[13] J. Bures, S. Lacroix, J. Lapierre, Appl. Opt., **22**, 1918, 1983.

[14] R. G. Lamont, D. C. Johnson, K. O. Hill, Appl. Opt., **24**, 327, 1985.

[15] X. H. Zheng, A. W. Snyder, Elect. Lett., **23**, 182, 1987.

[16] F. P. Payne, C. D. Hussey, M. S. Yataki, Elect. Lett., **21**, 561, 1985.

[17] A. W. Snyder, X. Zheng, Elect. Lett., **21**, 1079, 1985.

[18] X. Zheng, Elect. Lett., **22**, 804, 1986.

[19] X. Zheng, A. W. Snyder, Elect. Lett., **23**, 182, 1987.

[20] A. C. Boucouvalas, G. Georgiou, Elect. Lett., **21**, 864, 1985.

[21] K. P. Jedrezejewski, F. Martinez, J. D. Minelly, C. D. Hussey, F. P. Payne, Elect. Lett., **22**, 105, 1986.

[22] A. C. Boucouvalas, G. Georgiou, Elect. Lett., **21**, 1033, 1985.

[23] K. O. Hill, D. C. Johnson, R. G. Lamont, Proc. SPIE, **574**, 92, 1985.

[24] C. M. Lawson, P. M. Kopera, T. Y. Hsu, V. J. Tekippe, Elect. Lett., **20**, 963, 1984.

[25] F. Bilodeau, D. C. Johnson, S. Faucher, K. O. Hill, Proc. SPIE, **988**, 2, 1988.

[26] T. A. Birks, P. St. J. Russell, D. O. Culverhouse, J. Lightwave Tech., **14**, 2519, 1996.

[27] L. C. Bobb, H. D. Krumboltz, P. M. Shankar, Opt. Lett., **16**, 112, 1991.

[28] D. T. Cassidy, D. C. Johnson, K. O. Hill, Appl. Opt., **24**, 945, 1985.

[29] A. W. Snyder, J. D. Love, Optical Waveguide Theory, Chapman and Hill, London, 1983.

[30] S. Lacroix, R. Bourbonnais, F. Gonthier, J. Bures, Appl. Opt., **25**, 4421, 1986.

[31] N. L. Alpert, W. E. Keiser, H. A. Szymanski, IR: Theory and Practice if Infrared Spectroscopy, 2nd ed., Plenum, New York, 1970.

[32] S. Simhony, E. M. Kosower, A. Katzir, Appl. Phys. Lett., **49**, 253, 1986.

[33] H. Tai, H. Tanaka, T. Yoshino, Opt. Lett., **12**, 437, 1987.

[34] A. Messica, A. Greenstein, A. Katzir, Appl. Opt., **35**, 2274, 1996.

[35] V. Ruddy, B. D. MacCraith, J. A. Murphy, J. Appl. Phys., **67**, 6070, 1990.

[36] B. D. Gupta, A. Sharma, C. D. Singh, Int. J. Optoelect., **8**, 409, 1993.

[37] B. D. Gupta, C. D. Singh, Appl. Opt., **33**, 2737, 1994.

[38] F. de Fornel, C. M. Ragdale, R. J. Mears, IEE Proceedings H, **131**, 221, 1984.

[39] S. Albin, A. C. Lavarias, J. Zheng, Elect. Lett., **33**, 1815, 1997.

[40] A. C. Lavarias, J. Zheng, S. Albin, "Anomalous Dispersion in Biconically Tapered Optical Fibers", OSA/IEEE LEOS Technical Digest, 12th International Conference on Optical Fiber Sensors, **16**, October 28-31, 1997, OThC9-1, 440.

VITA

Arnel Cabasa Lavarias

Address: 869 Strickland Blvd., Virginia Beach, VA 23464

Education:

- B.S. in Electrical Engineering, Old Dominion University, Norfolk, VA, May 1993.
- M.S. in Electrical Engineering, Old Dominion University, Norfolk, VA, May 1995.

Dr. Lavarias was the recipient of the NASA Graduate Student Researchers Program from 1993 to 1997. From 1993 to 1996, he was also the recipient of the Virginia Space Grant Consortium Aerospace Graduate Research Fellowship. He has published several journal and conference papers related to fiber optic sensors, and he has also published a book chapter on research related to fiber optic temperature sensing using Y_2O_3:Eu^{3+}. His main research interest is in fiber optic sensors and optical spectroscopy.